Applications of vacuum vapor deposition for perovskite solar cells: A progress review

Hang Li[1], Mingzhen Liu[2], Meicheng Li[3], Hyesung Park[4], Nripan Mathews[5], Yabing Qi[6], Xiaodan Zhang[7], Henk J. Bolink[8], Karl Leo[9], Michael Graetzel[10] and Chenyi Yi[1] ✉

ABSTRACT

Metal halide perovskite solar cells (PSCs) have made substantial progress in power conversion efficiency (PCE) and stability in the past decade thanks to the advancements in perovskite deposition methodology, charge transport layer (CTL) optimization, and encapsulation technology. Solution-based methods have been intensively investigated and a 25.7% certified efficiency has been achieved. Vacuum vapor deposition protocols were less studied, but have nevertheless received increasing attention from industry and academia due to the great potential for large-area module fabrication, facile integration with tandem solar cell architectures, and compatibility with industrial manufacturing approaches. In this article, we systematically discuss the applications of several promising vacuum vapor deposition techniques, namely thermal evaporation, chemical vapor deposition (CVD), atomic layer deposition (ALD), magnetron sputtering, pulsed laser deposition (PLD), and electron beam evaporation (e-beam evaporation) in the fabrication of CTLs, perovskite absorbers, encapsulants, and connection layers for monolithic tandem solar cells.

KEYWORDS

Perovskite solar cells, vacuum vapor deposition, thermal evaporation, stability, efficiency, industrial manufacture.

Global warming, environmental pollution, and population growth indicate the necessity of developing abundant renewable energy sources to meet the rapidly growing energy demand. Photovoltaics (PVs) are an eco-friendly power generation technology. As the 3rd generation PV technology, perovskite solar cells (PSCs) have excellent characteristics like high optical absorption coefficient, tunable bandgap, high defect tolerance, and long charge diffusion length, which together with low fabrication costs render it an ideal PV technology for solar harvesting[1]. Record power conversion efficiency (PCE) as high as 25.7% and 31.3% were achieved on single-junction and perovskite-silicon tandem devices, surpassing other thin-film PV technologies[2]. The outstanding progress can be attributed to significant advancements in fabricating high-quality perovskite absorbers and well-performing charge transport materials.

Morphology, crystallinity, stoichiometry, defect density, absorber thickness, and ion migration activation energy all influence the key processes in the solar cells, such as photon absorption, charge transport, and recombination kinetics within the perovskite layer, which together with the charge extraction process in charge transport layers (CTLs) pose a major impact on the performance

and stability of PSCs[3]. In the past decade, tremendous efforts have been put in the development of deposition protocols of perovskite absorbers and functional layers. Solution-based protocols such as spin coating, blade coating, slot-die coating, spray coating, inkjet printing, and drop casting have already been widely investigated in the past decade. Thanks to the advancements in crystallization strategies including antisolvent dripping, solvent engineering, additive doping, seed-assisted growth, interface engineering, and passivation, the efficiency and stability of solution-based PSCs have developed rapidly.

On the other hand, vapor deposition protocols were less studied in early years but have received increasing attention from researchers worldwide in recent years because of their compatibility with scalable industrial fabrication and facile integration with tandem solar cell structures. A PCE as high as 24.4% was reported based on vacuum deposited perovskite absorbers in 2022[4]. An in-depth investigation of the crystallization process of vacuum deposited perovskites enables a deeper understanding of the perovskite properties. In addition, vapor deposition can be applied in fabricating charge transport layers, back electrodes, and encapsulants, which are fundamentally important for device performance as well as critical for technological translation.

[1]State Key Laboratory of Power System, Department of Electrical Engineering, Tsinghua University, Beijing 100084, China; [2]School of Materials and Energy, University of Electronic Science and Technology of China, Chengdu 611731, China; [3]State Key Laboratory of Alternate Electrical Power System with Renewable Energy Sources, School of New Energy, North China Electric Power University, Beijing 102206, China; [4]Department of Materials Science and Engineering, Graduate School of Semiconductor Materials and Devices Engineering, Perovtronics Research Center, Low Dimensional Carbon Materials Center, Ulsan National Institute of Science and Technology, Ulsan 44919, Republic of Korea; [5]Energy Research Institute @ NTU (ERI@N), Nanyang Technological University, Singapore 637553, Singapore; [6]Energy Materials and Surface Sciences Unit (EMSSU), Okinawa Institute of Science and Technology Graduate University (OIST), 1919-1 Tancha, Onna-son, Okinawa 904-0495, Japan; [7]Institute of Photoelectronic Thin Film Devices and Technology, Renewable Energy Conversion and Storage Center, Solar Energy Conversion Center, Nankai University, Tianjin 300350, China; [8]Instituto de Ciencia Molecular, Universidad de Valencia, C/Catedrático J. Beltrán 2, 46980 Paterna, Spain; [9]Integrated Centre for Applied Physics and Photonic Materials (IAPP) and the Centre for Advancing Electronics Dresden (CFAED), Technische Universitaet Dresden, 01062 Dresden, Germany; [10]Laboratory of Photonics and Interfaces(LPI), Ecole Polytechnique Federale de Lausanne, 1015 Lausanne, Switzerland
Address correspondence to Chenyi Yi, yicy@mail.tsinghua.edu.cn

Vapor deposition offers several advantages compared with solution-based methods: (1) Large-area uniformity. Precursors are vaporized with uniform partial pressures in the vacuum chamber, which guarantees the large-area uniformity of the deposited layer. In addition, the precursor deposition velocity and thickness can be precisely controlled[3]. (2) Elimination of solvents. In solution-based methods, non-benign and high boiling point organic solvents are usually employed. Coordinating solvents such as dimethyl sulfoxide (DMSO), N,N'-dimethylformamide (DMF) are needed to dissolve the inorganic Pb and Cs halide salts. After annealing, traces of the used solvents remain in the perovskite layer, which have a detrimental effect on the underlying layers and may deteriorate the device efficiency and stability[5]. However, for vacuum deposition methods, commonly-used organic solvents can be avoided, which may benefit the device efficiency and stability. In addition, the toxicity concerns and recycling issues of waste solvents pose a major challenge for the industrial manufacture of solution-based PSCs. (3) Conformal growth on textured substrates. Vapor deposition methods are suitable for depositing uniform, pinhole-free and conformal films on textured surfaces such as pyramidal, inverted pyramidal, and sinusoidal microstructures[6]. This feature is advantageous when fabricating monolithic tandem devices by depositing perovskite solar cells on textured silicon cells. The textured surface of Si cell provides superior light trapping and reflection reduction and enhances photocurrent generation compared to planar surface. (4) Compatibility with the existing PV manufacturing lines. Vapor deposition protocols such as thermal evaporation and magnetron sputtering have already been widely used in the manufacture of other thin-film PV technologies such as CdTe and CIGS[3]. Similar equipment can be applied to the fabrication of PSCs after necessary modifications.

In this review, we discuss the applications of several vapor deposition methods, namely vacuum thermal evaporation, chemical vapor deposition (CVD), atomic layer deposition (ALD), pulsed laser deposition (PLD), e-beam evaporation, and magnetron sputtering used to prepare PSCs. This includes the deposition of the perovskite absorbers, the electron and hole transport layers (ETLs and HTLs, respectively), thin-film encapsulants, and charge recombination layers employed in the case of monolithic tandem solar cells. We analyze the strengths and weaknesses of each method and outline potential application scenarios in PSC fabrication. The future development opportunities and challenges for all-vacuum deposited PSCs for scalable industrial manufacture are also briefly reviewed.

1 Thermal evaporation

Thermal evaporation is the earliest developed and most widely-used physical vapor deposition (PVD) technology where the raw materials are thermally heated, vaporized, and deposited onto the substrate monitored by one or more quartz crystal microbalance (QCM) sensors in a vacuum chamber[7]. Thermal evaporation has already been widely applied in semiconductor industry including thin-film PVs, large-area OLEDs, and photodetectors[8–10]. The maturity and reliability of thermal evaporation render it to be a competitive technique for the commercial fabrication of PSC modules. It can be used to fabricate perovskite absorbers and CTLs. Several thermal evaporation methods were explored to deposit perovskite layers, such as coevaporation, sequential evaporation, single-source evaporation, and hybrid vapor–solution deposition[3].

1.1 Thermal evaporation for perovskite absorbers

1.1.1 Coevaporation method

Multisource coevaporation is a commonly-used evaporation method to deposit perovskite absorbers where the metal halide and ammonium salt are vaporized and deposited simultaneously[1], which consists of five fundamental processes including raw material sublimation, spatial transport, molecular absorption and desorption, diffusion into the film, and precursor reaction and nucleation (Figure 1a)[1]. This method was first employed to deposit metal halide perovskites in 1997 by Era et al.[11]. In 2013, Liu et al. reported a dual-source coevaporation technique to fabricate perovskite films composed of $MAPbI_xCl_{3-x}$[12]. Lead chloride ($PbCl_2$) and methylammonium iodide (MAI) were sublimed simultaneously and by rotating the water-cooled substrate, perovskite films with uniform thickness and good morphology were successfully deposited. They optimized the composition of the perovskite film by adjusting the evaporation rate of each source and a PCE over 15% was achieved with a planar structure device. Soon after the group of Bolink showed that $MAPbI_3$ could also be obtained by coevaporation of MAI and PbI_2[13]. They reported a PCE of 15 % on small area cells and 11% on 1 cm^2 cells[14]. In 2020, Li et al. demonstrated the large-area scalability of thermally co-evaporated $MAPbI_3$ by realizing a mini-module (Figures 1b and 1c)[15]. They coevaporated MAI and lead iodide (PbI_2) to fabricate $MAPbI_3$ absorbers followed by 20 mM potassium acetate (KAc) and MAI post-treatment and achieved PCEs of 20.28% and 18.13% with aperture areas of 0.16 cm^2 and 21 cm^2 with a device structure of FTO/SnO$_2$/PCBM/MAPbI$_3$/Spiro-OMeTAD/Au. Later they demonstrated the remarkable thermal stability of the thermal evaporated $MAPbI_3$ devices (Figure 1d)[16]. The unencapsulated PSCs can maintain more than 95% and 80% of their initial PCE after 1000 hours and 3600 hours, respectively under continuous thermal aging at 85 °C, much better than the solution-processed PSCs with the same composition, which is attributed to the compact and almost strain-stress-free perovskite films fabricated by thermal evaporation. Borchert et al. studied the evaporation behavior of MAI[17]. They found that the QCM was sensitive to the impurities in MAI flux including MAH_2PO_3 and MAH_2PO_2, making the recorded evaporation rate unreliable. Once an accurate control of MAI was achieved, the performance and reproducibility of the fabrication could be improved.

Apart from methylammonium (MA) based perovskites, coevaporation can also be used to fabricate formamidinium (FA) based perovskites. In 2017, group of Johnston first coevaporated formamidinium iodide (FAI) and PbI_2 to deposit homogeneous $FAPbI_3$ films over large areas (Figure 1e)[18]. Later they reported PSCs composed of $FA_{0.83}Cs_{0.17}PbI_3$ by coevaporating cesium iodide (CsI), PbI_2, $PbCl_2$, and FAI (Figure 1f)[19]. A reduced nonradiative recombination was observed with the incorporation of chlorine and a PCE of 19.3% was achieved. Chiang et al. coevaporated PbI_2, cesium bromide (CsBr) and FAI to fabricate $FA_{0.7}Cs_{0.3}Pb(I_{0.9}Br_{0.1})_3$ perovskite films with good morphological, structural, and optoelectronic properties[20]. They revealed that coevaporation was sensitive to a range of parameters, including substrate, annealing temperature, evaporation rates, and source purity. They also found that an excess of PbI_2 was critical for improving the efficiency and stability of PSCs. A stabilized power output of 18.2% was achieved with 5% PbI_2 excess. Gil-Escrig et al. coevaporated MAI, FAI and PbI_2 to deposit cubic-phase $FA_{1-x}MA_xPbI_3$ films, and they found the amount of MA$^+$ incorporated into the perovskite was unvaried with increasing MAI
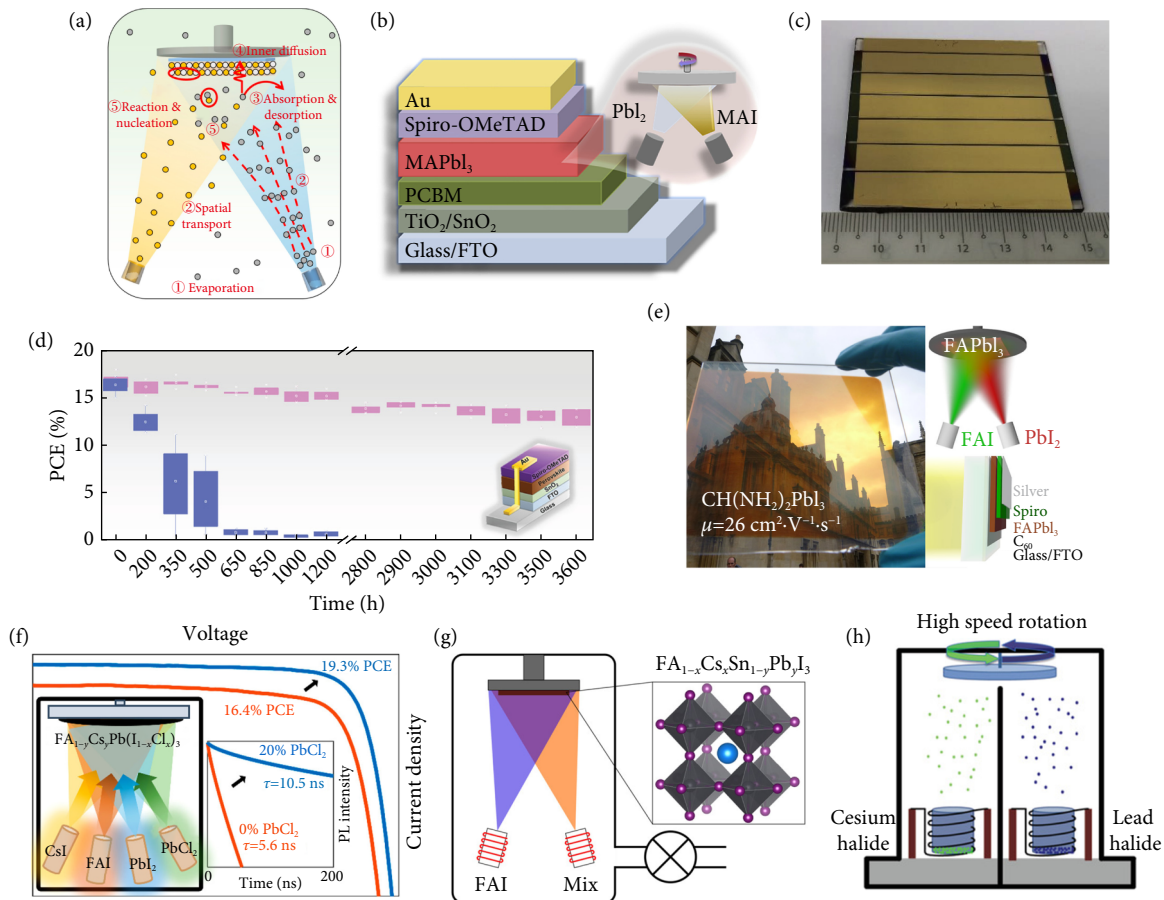
Fig. 1 Thermal coevaporation protocol for perovskite films. (a) Schematic illustration of the dual-source coevaporation method (reprinted with permission from ref. [1], © 2022 The Authors). **(b** and **c)** Device structure of **(b)** coevaporated MAPbI₃ PSCs and **(c)** corresponding modules (reprinted with permission from ref. [15] © 2020 Elsevier Inc). **(d)** Long-term thermal stability of coevaporated MAPbI₃ PSCs. (reprinted with permission from ref. [16] © 2021 Wiley-VCH). **(e)** Device structure and photograph of the thermally evaporated large-area FAPbI₃ PSCs. (reprinted with permission from ref. [18], © 2017 American Chemical Society). **(f)** Schematic illustration and corresponding J–V curves of quadruple-source coevaporation for FA-based perovskite films (reprinted with permission from ref. [19], © 2022 The Authors). **(g)** Schematic illustration of coevaporation of FAI and $Cs_xSn_yPbI_{2+x+2y}$ molten salt for Sn-based PSCs (reprinted with permission from ref. [24], © 2019 American Chemical Society). **(h)** Schematic illustration of thousand-layer rapid alternative deposition method for inorganic perovskite films (reprinted with permission from ref. [26] © 2019 Wiley-VCH).

evaporation rate[21]. As a result, they achieved a PCE of 18.8%. Later they adopted a four-source coevaporation strategy to evaporate wide-bandgap PSCs[22]. They adjusted the deposition rate of lead bromide ($PbBr_2$) to tune the bandgap and PSCs showed efficiency up to 16.8% with bandgap at 1.75 eV. In 2019, Qi and his group used coupled thermogravimetry-mass spectrometry analysis and found that formamidinium based lead halide perovskites could degrade into sym-triazine ($C_3H_3N_3$) and hydrogen cyanide (HCN)[23]. Later 2022, similar findings were also reported by group of Leo. They concluded that the source temperature of FAI has to be kept as low as possible to avoid significant decomposition and the formation of unwanted byproducts.

Coevaporation for tin (Sn) and cesium (Cs) based perovskite films were also studied in the past few years. In 2019, Snaith and his group reported a strategy of coevaporating FAI and mixed melting halides to deposit $FA_{1-x}Cs_xSn_{1-y}Pb_yI_3$ (Figure 1g)[24]. They co-melted CsI, PbI_2, tin iodide (SnI_2) and evaporated the mixed molten salt in a single crucible. They found the inclusion of tin fluoride (SnF_2) into the molten salt can improve the perovskite quality and achieved a stabilized power output (SPO) of ~10%. Later in 2020, Igual-Muñoz et al. coevaporated PbI_2, SnI_2, SnF_2 and FAI to produce $FAPb_{0.5}Sn_{0.5}I_3$[25]. They achieved a PCE of

13.98% with a bandgap of 1.23 eV. Inorganic perovskites such as $CsPbI_3$ and $CsPbI_2Br$ were also explored via thermal evaporation. In 2019, Lin et al. proposed a thousand-layer rapid alternative deposition method to fabricate $CsPbI_2Br$ film where the vacuum chamber was divided into two parts by a baffle (Figure 1h)[26]. Under this condition, the individual evaporation rate of both precursors can be precisely controlled by QCMs, making it feasible to control the composition of the evaporated films. Vaynzof and her group doped phenylethylammonium iodide (PEAI) into the coevaporated $CsPbI_3$ perovskite films[27]. They found the microstructure and crystal orientation improved significantly after the addition of PEAI and achieved a PCE of 15%. Later the same team produced multiple quantum wells (MQWs) with attractive optical properties by alternative evaporation of $CsPbBr_3$ perovskite thin films and 1,3,5-tris(2-N-phenylbenzimidazolyl) benzene (TPBi) barrier layers[28].

Although coevaporation can produce high-quality perovskite films and has been studied thoroughly, it has several shortcomings that may restrict the PSC performance and reproducibility. Firstly, because of the high volatility of ammonium salts, their vapor partial pressure is much higher than that of metal halides[29]. While the volatilization points of metal halides are much higher than that of

ammonium salts, the high crucible temperature of metal halide can affect the partial pressure of the ammonium molecules within the chamber, making the evaporation difficult to control. Secondly, it is difficult to monitor the evaporation rate of multiple precursors with a single QCM, making it unable to identify the individual evaporation rate of precursors, leaving a negative influence on reproducibility[26]. Lastly, it is reported that a small amount of the ammonium salt may remain in the chamber after evaporation, which may re-evaporate during the next evaporation process[30]. Such remnant precursors can affect the composition of the evaporated perovskite, reducing the batch-to-batch reproducibility of evaporated PSCs.

1.1.2 Sequential evaporation method

Compared with the multisource coevaporation, sequential evaporation avoids the risk of mutual interference by evaporating precursors separately or in different vacuum chambers, which can significantly improve the batch-to-batch reproducibility of the experiment. In addition, the evaporation rate of the metal halide and the ammonium salt can be monitored by the QCM, and thus, the film thickness of each precursor can be controlled much more precisely[31]. In recent years, PSCs fabricated by sequential evapo-

ration exhibited a higher efficiency than multisource coevaporation (Figure 2a)[32]. In 2021, Feng et al. reported a layer-to-layer deposition technique by evaporating PbI_2, FAI, and CsI sequentially, followed by thermal annealing in vacuum at 60 °C for 30 min (Figure 2d)[33]. Small-area PSCs achieved a champion efficiency of 21.32% and large-area perovskite films on rigid (400 cm²) and flexible (300 cm²) substrates were fabricated with uniform thickness (Figure 2e), demonstrating the large-area high-throughput capability of sequentially evaporated PSCs. The thermally evaporated PSCs with N,N'-Di(1-naphthyl)-N,N'-diphenyl-(1,1'-biphenyl)-4,4'-diamine (NPB) as hole transport material (HTM) showed negligible aging after stored in air for 189 days (Figure 2f). Park et al. proposed a highly oriented butylammonium Ruddlesden–Popper (RP) perovskite as a surface passivation layer via vacuum deposition (Figures 2b and 2c)[34]. The RP perovskite passivation layer can considerably reduce the trap density of bulk perovskite and enhance the charge transport. Combined with the sequentially evaporated $MAPbI_3$ perovskite absorber, they achieved a champion PCE of 21.4% and improved thermal stability and humidity stability.

Although sequential evaporation can fabricate large-area perovskite films with good uniformity, their efficiency still lags far behind that of the solution-processed PSCs. Therefore, it is
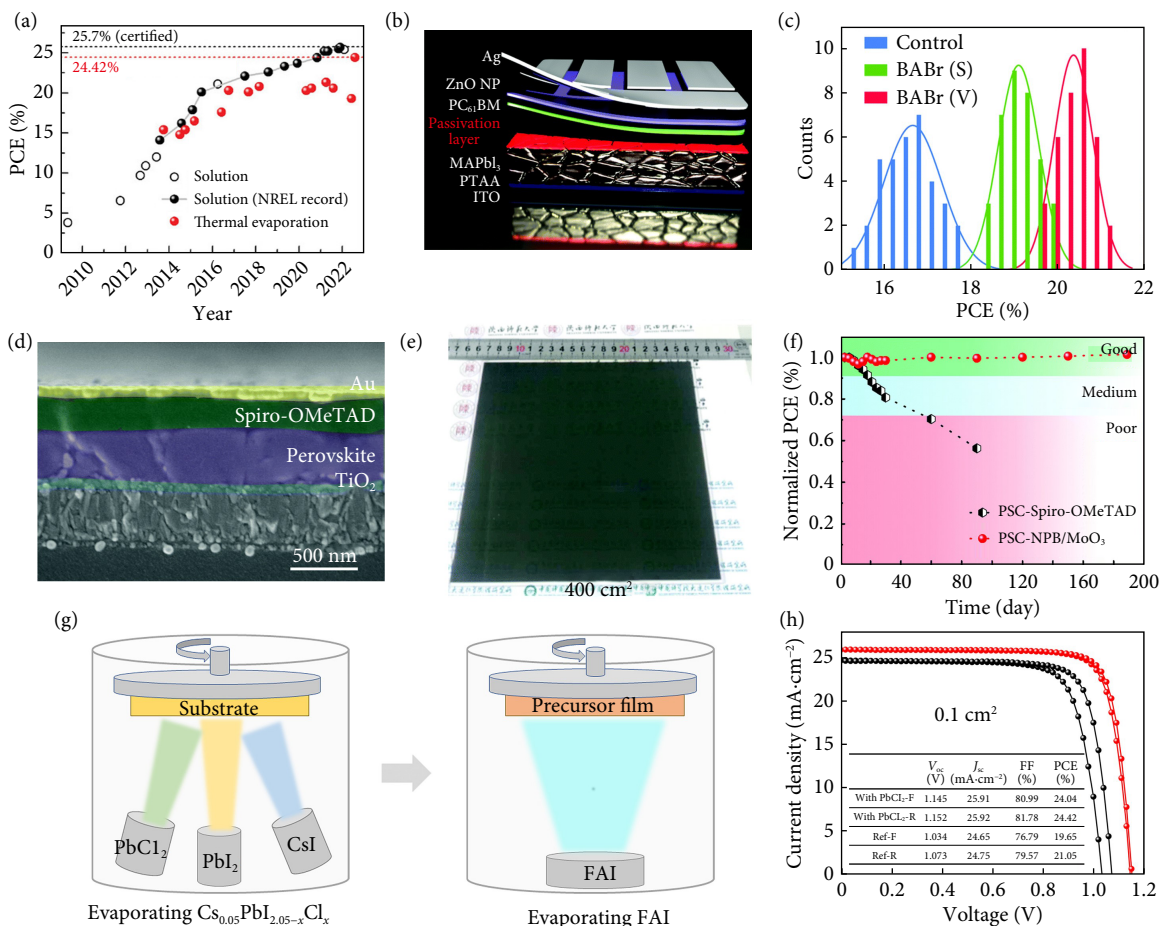

Fig. 2 Sequential evaporation protocol for perovskite films. (a) Advancements of efficiency in thermally evaporated PSCs (reprinted with permission from ref. [121], © 2022 Wiley-VCH). **(b and c)** Device structure of sequentially evaporated $MAPbI_3$ PSCs **(b)** and PCE distributions via different post-treatment **(c)** (reprinted with permission from ref. [33], © 2022 The Royal Society of Chemistry). **(D)** Cross-sectional SEM images of sequentially evaporated $Cs_xFA_{1-x}PbI_3$ films. **(e)** Photograph of evaporated 400 cm² $FAPbI_3$ film on glass substrate. **(f)** Environmental stability of unencapsulated PSCs with NPB or spiro-OMeTAD as HTL. The devices were exposed to the atmospheric environment of 35% humidity in the dark. **(d–f)** Reprinted with permission from ref. [32], © 2021 The Royal Society of Chemistry. **(g)** Schematic illustration of the Cl-alloy mediated sequential evaporation method. **(h)** J–V curve and corresponding parameters of Cl-alloy mediated PSC and reference PSC. **(g and h)** Reprinted with permission from ref. [4], © 2022 The Authors, some rights reserved; exclusive licensee American Association for the Advancement of Science.

imperative to develop advanced evaporation techniques to fabricate high-efficiency PSCs which are competitive with solution-processed PSCs. In 2022, Li et al. reported a Cl-containing alloy-mediated sequential evaporation method to fabricate MA-free PSCs with high efficiency and good stability[4]. They coevaporated $PbCl_2$, PbI_2, and CsI to form the Cl-alloy mediated film, followed by the vacuum deposition of the FAI layer (Figure 2g) and afterwards the precursor films were thermally annealed at $170\,^\circ C$ in ambient air for FAI diffusion and perovskite crystallization. They demonstrated that the Cl-alloy mediated lead halide film ($Cs_{0.05}PbI_{2.05-x}Cl_x$) exhibited better crystallinity and a highly vertical preferential orientation compared with the reference film ($Cs_{0.05}PbI_{2.05}$). In addition, the incorporated chlorine can accelerate the diffusion of FAI and the crystallization of perovskite. They achieved PCEs of 24.42%, 23.44% and 19.87% for 0.1 cm², 1 cm² and 14.4 cm² PSCs, respectively, with a device structure of $FTO/SnO_2/Cs_{0.05}FA_{0.95}PbI_3/Spiro$-OMeTAD/Au (Figure 2h), which is the highest PCE of vacuum evaporated PSCs to date, demonstrating the feasibility of high-efficiency PSCs via the sequential vacuum evaporation method. Later the same team reported a molten salt evaporation strategy for fabricating PSCs[35]. The molten salt can simplify the evaporation process and stabilize the evaporation rate, which greatly improve the reproducibility. The perovskite compositions can be tuned by adjusting the composition of the molten salt.

1.1.3 Single-source evaporation method

The stoichiometry of evaporated perovskite films is crucial to the optoelectronic performance of PSCs. Numerous factors such as heating temperature, vacuum pressure, and dissemination and quantity of evaporated materials can influence the evaporation rate and thereby change the stoichiometry of deposited films, heavily influencing the reproducibility and efficiency of evaporated PSCs[36]. For the coevaporation process, the correct ratio of evaporation rates is difficult to control during the lengthy coevaporation process. For the sequential evaporation, it is time-consuming to deposit different precursors separately.

Another method in which a preformed perovskite powder or film is sublimed was first described by Mitzi et al. in 1999[37], and adopted by Longo et al. to prepare perovskite solar cells[38]. When powders are used, the method is now referred to as single-source evaporation, where the precursors are mixed up, ball-milled to powders, and sublimed in vacuum to deposit perovskite layers[39]. The stoichiometry of the deposited perovskite can be tuned by simply adjusting the stoichiometry of raw materials, being more
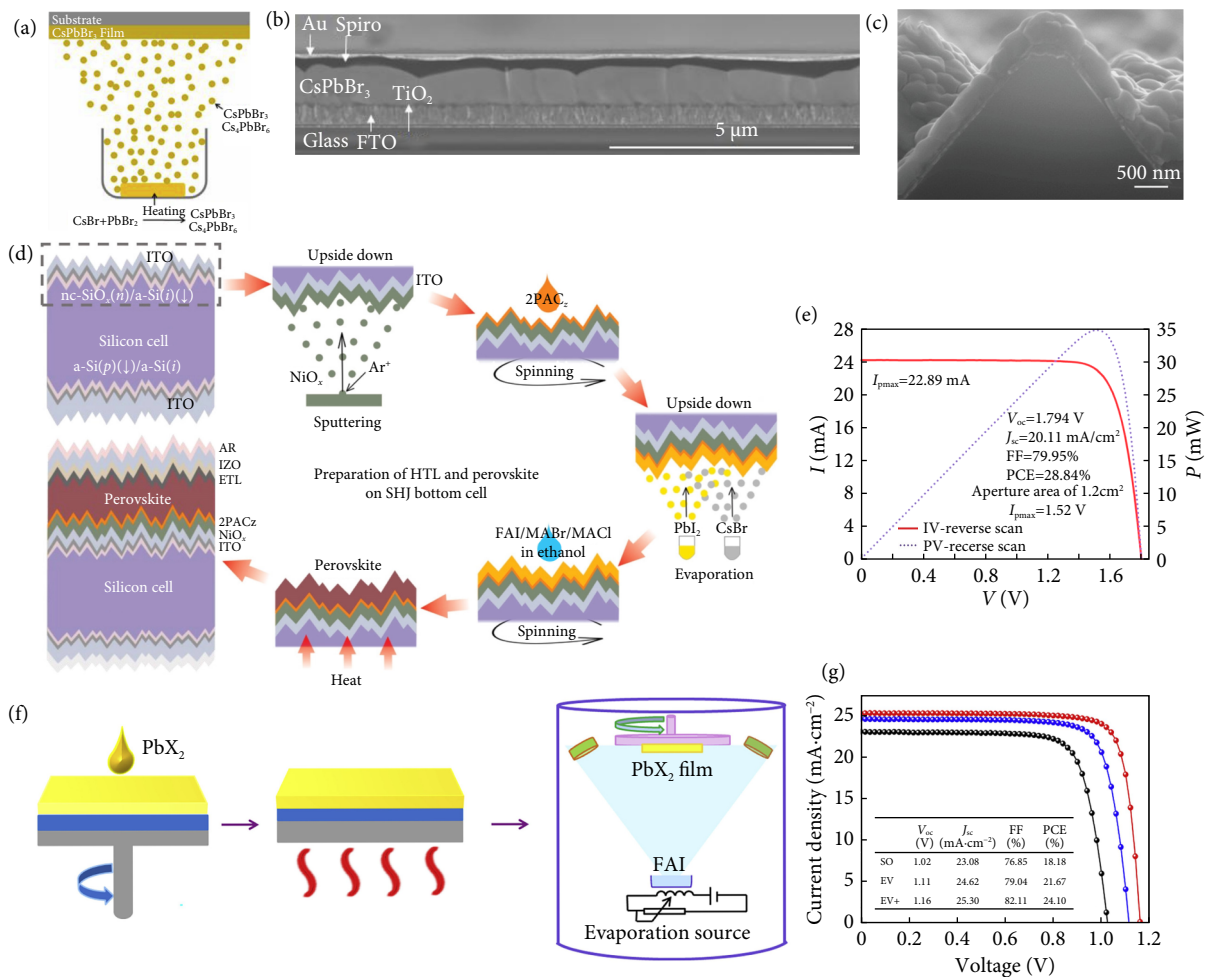

Fig. 3 Single-source evaporation and vapor-solution hybrid protocols for perovskite films. (a) Schematic illustration of single-source evaporation for $CsPbBr_3$ films. **(b)** Corresponding cross-sectional SEM images of $CsPbBr_3$ film. (**a** and **b**) Reprinted with permission from ref. [39], © 2019 Elsevier B.V. **(c)** Cross-sectional SEM image of the perovskite deposited conformally on a fully-textured silicon cell. (reprinted with permission from ref. [42], © 2021 Wiley-VCH). **(d)** Schematic illustration of vapor–solution deposition method on fully-textured silicon cell. **(e)** J–V curve and corresponding parameters of tandem cells with an aperture area of 1.2 cm². (**d** and **e**) Reprinted with permission from ref. [43], © 2022 Wiley-VCH. (**f** and **g**) Schematic illustration of vapor-solution hybrid method for MA-free PSCs **(f)** and J–V curve and corresponding parameters of PSCs **(g)** (reprinted with permission from ref. [44], © 2022 Elsevier Inc.)

convenient than coevaporation and less time-consuming than sequential evaporation[40].

Li et al. fabricated efficient $CsPbBr_3$ inorganic PSCs via single-source evaporation (Figures 3a and 3b)[41]. CsBr and $PbBr_2$ powders were mixed and pressed into tablets for evaporation. They found although the melting point of CsBr (630 °C) is much higher than that of $PbBr_2$ (370 °C), the materials can be evaporated and deposited onto the substrate at 450 °C in vacuum. By optimizing the molar ratio of $PbBr_2$ to CsBr in the mixture, they achieved a PCE of 8.65% with an open circuit voltage (V_{oc}) of 1.37 V and bandgap of 2.3 eV with uniform perovskite thickness. Later Nasi et al. found that the single-source evaporated $CsPbBr_3$ layer consisted of a mixture of $CsPbBr_3$, $CsPb_2Br_5$ and Cs_4PbBr_6 with a vertical composition gradient[42]. They demonstrated that $CsPb_2Br_5$ and Cs_4PbBr_6 phases can be converted to $CsPbBr_3$ in low humidity or upon mild thermal treatments, resulting in smooth and pinhole-free films with good light absorption properties. Apart from inorganic PSCs, single-source evaporation can also be used to fabricate organic-inorganic hybrid perovskites. In 2022, Klipfel et al. reported the fabrication of pure-phase $Cs_xFA_{1-x}PbI_3$ and $FAPbI_3$ perovskite films from pre-synthesized perovskite powders[43]. They first used room temperature precipitation method to fabricate δ-$FAPbI_3$ and δ-$Cs_xFA_{1-x}PbI_3$ powders, followed by vacuum thermal evaporation to deposit uniform and pinhole-free perovskite films.

1.1.4 Hybrid vapor–solution deposition

Hybrid vapor–solution deposition methods are two-step deposition methods which combine the solution method with the vapor deposition method. The hybrid vapor-solution deposition takes advantage of the solution processing in additive doping, interface engineering, and crystallization control, and the vacuum deposition processing in film uniformity and processing up-scalability[3]. Vacuum evaporation of metal halide films is easier than ammonium salt deposition. Evaporating a uniform lead halide skeleton followed by solution-processed ammonium salt penetration is a good way to build high-quality perovskite layers. Li et al. reported a hybrid vapor–solution deposited p-i-n perovskite top cell on fully textured c-Si solar cell to construct conformal-grown monolithic tandem cells (Figure 3c)[44]. They coevaporated CsBr and PbI_2 on the textured substrate, followed by a spin-coating procedure of a mixture of FABr and FAI with a molar ratio of 1:6.98. With the aid of hybrid vapor–solution deposition method, perovskite layer can conformally cover the top and valley of the pyramids, reducing the shunt paths and fully utilizing the light-trapping ability of the textured structure. They achieved a PCE of 27.48% and the tandem cells realized long-term stability over 10,000 hours in the nitrogen environment. Later, Liu et al. adopted a similar technique to fabricate large-area monolithic tandem cell (Figure 3d). They first deposited NiO_x/2PACz as HTL, on which a $Cs_xPbI_2Br_x$ film was coevaporated, followed by spin-coating deposition of FAI/MABr/MACl in ethanol. They achieved a PCE of 28.84% with a 1.2 cm² aperture area (Figure 3e), demonstrating the feasibility of hybrid vapor-solution deposition method on textured substrates[45].

Spin-coating of the FAI solution usually results in poor morphology with pinholes, increasing the difficulty of fabricating solution-processed FA-based PSCs with high efficiency. On the other hand, vacuum thermal evaporation of FAI can avoid this issue, obtaining highly uniform FAI layers and high-quality perovskite films after thermal annealing. Recently, Yi et al. reported a morphology engineering method by spin-coating a solution composed of CsBr, PbI_2 and $PbCl_2$ followed by vacuum evaporation of FAI to fabricate MA-free perovskite films (Figure 3f)[46]. Thermal evaporation can produce homogeneous FAI layers with controllable thickness, which facilitates the subsequent chemical reaction between FAI and lead halide, resulting in perovskite films with good morphology. They achieved a PCE of 24.1% and 22.8% for 0.1 cm² and 1 cm² devices, respectively (Figure 3g), and the PSCs exhibited excellent stability with negligible efficiency decline after 20000 hours storage in dry air or 1000 hours exposed to 50% humidity, demonstrating the good quality of the vacuum-deposited FAI layer.

1.2 Thermal evaporation for CTLs

CTLs are essential for fabricating high-efficiency PSCs which require good band alignment, good charge selectivity, high conductivity, uniform and dense film morphology, and low parasitic absorption[47]. Early in 2014, Polander et al. studied a variety of vapor-deposited HTMs and their potential in $MAPbI_{3-x}Cl_x$ PSCs[48]. They addressed the importance of the energy level alignment between HTM and perovskite layer. Organic HTMs like 2,2′,7,7′-tetrakis(N,N-di-p-methoxyphenylamine)-9,9′-spirobifluorene (spiro-OMeTAD) is the benchmark HTM widely-used for PSCs. Nevertheless, most of the reported spiro-OMeTAD and its derivatives in the literature were deposited by spin-coating, which is not practical for either large-area devices or industrial scalable fabrication. Additionally, neat spiro-OMeTAD suffers from low hole mobility and requires doping by some hygroscopic dopants like lithium bis(trifluoromethanesulfonyl)imide salt (LITFSI), which can migrate to the underlying layers and have a detrimental effect on the device stability[49]. On the other hand, thermal evaporation is suitable for depositing large-area layers with good morphology and uniformity which has great potential in depositing organic HTMs. In 2022, Du et al. reported a solvent-annealing assisted thermal evaporation approach to evaporate undoped spiro-OMeTAD (Figure 4a)[50]. They found that the optimum thickness of spiro-OMeTAD deposited by coevaporation is ~70 nm, much smaller than that of solution-processed spiro-OMeTAD at ~250 nm. Combined with the chlorobenzene post-treatment to induce partial dissolution and molecular rearrangement, a champion efficiency over 20% was achieved and PSCs showed prolonged environmental stability with more than 85% of initial PCE after 2500 hours in ambient air. Park and his group reported thermally evaporated fluorinated analogue spiro-OMeTAD (spiro-mF) for all-vacuum processed p-i-n type PSCs[51]. They found that spiro-mF exhibited a suitable energy level alignment, improved crystallinity along the π–π stacking direction, and uniform surface morphology compared to solution-processed spiro-mF or spiro-OMeTAD. Furthermore, the device performance and stability were notably improved. They also demonstrated the large-area scalability of the all-vacuum deposited PSCs with a device structure of ITO/spiro-mF/$MAPbI_3$/$PC_{61}BM$/ZnO/Ag. 2,2′,7,7′-tetra(N,N-di-tolyl)amino-9,9-spiro-bifluorene (Spiro-TTB) as another spiro-based derivative was also reported for thermal evaporation[44]. Vaynzof and her group obtained a PCE of 16.6% for fully-evaporated $Cs_{0.1}FA_{0.9}PbI_{2.9}Br_{0.1}$ PSCs[52]. They evaporated C_{60} as ETL and 2,2′-(perfluoronaphthalene-2,6-diylidene) dimalononitrile (F_6-TCNNQ) and spiro-TTB as HTLs.

Apart from spiro-OMeTAD and its derivatives, polymers such as poly(bis(4-phenyl)(2,4,6-trimethylphenyl)amine) (PTAA) is also commonly used organic HTM and can be produced via thermal evaporation. Tavakoli et al. evaporated 2~10 nm PTAA with a molecular weight of ~16 kDa as HTL[53]. They found the molecular weight before and after evaporation to be almost the same, indicating that the molecular structure of PTAA was not changed by
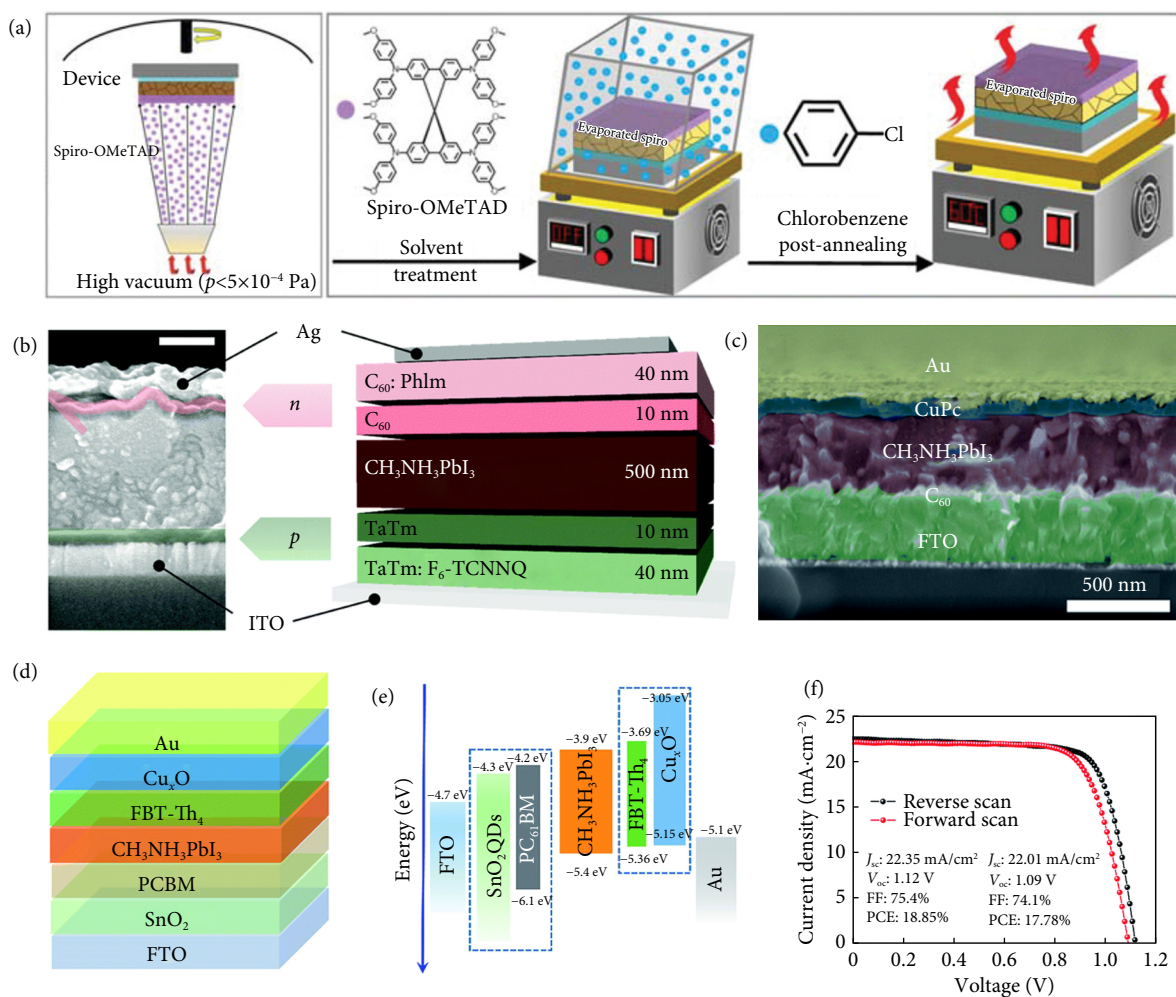
Fig. 4 Thermal evaporation for CTLs. (a) Schematic illustration of thermally evaporated spiro-OMeTAD and solvent treatment by chlorobenzene (reprinted with permission from ref. [48], © 2022 Wiley-VCH). **(b)** Cross-sectional SEM image and device structure of fully-evaporated inverted PSC (reprinted with permission from ref. [55] © 2016 The Royal Society of Chemistry). **(c)** Cross-sectional SEM image of PSC with thermally-evaporated CuPc as HTL (reprinted with permission from ref. [53], © 2015 The Royal Society of Chemistry). **(d, e** and **f)** Schematic illustration **(d)**, energy band diagram **(e)** and *J–V* curve **(f)** of PSCs with Cu$_x$O as HTL (reprinted with permission from ref. [54] © 2018 The Royal Society of Chemistry).

thermal evaporation. They vacuum deposited fullerene (C_{60}) and bathocuproine (BCP) as ETL, and achieved PCEs of 19.4% and 18.1% for 0.1 cm^2 and 1 cm^2 devices, respectively.

Inorganic or organic–inorganic hybrid hole transport materials (HTMs) including copper(I) thiocyanate (CuSCN), copper(I) phthalocyanine (CuPc), copper oxide (Cu$_x$O), copper(I) iodide (CuI) and nickel oxide (NiO$_x$) usually exhibit high mobility and low synthetic cost compared to their organic counterparts[54]. In addition, inorganic HTMs usually exhibit good thermal stability and moisture stability because of their inert chemical property and compact film morphology, which make them become ideal candidates for commercialization. Thermal evaporation can be adopted to deposit inorganic HTMs with high uniformity. Early in 2015, Ke et al. reported all-vacuum evaporated planar PSCs using CuPc as HTM (Figure 4c)[55]. They deposited a 60 nm CuPc film on a 370 nm evaporated perovskite film and achieved a PCE of 15.42% with a device structure of FTO/C_{60}/MAPbI$_3$/CuPc/Au. In 2018, Guo et al. reported an organic–inorganic integrated HTL composed of vacuum evaporated Cu$_x$O and solution-processed polymer FBT-Th4 and achieved a PCE of 18.85% (Figures 4d–4f)[56]. Compared to the devices using spiro-OMeTAD as HTL, the PSCs with FBT-Th4/Cu$_x$O exhibited enhanced stability at 70%–80%

humidity, which indicates Cu$_x$O layer successfully blocks the water molecule penetration and protects the underlying perovskite layer from water deterioration.

C_{60} and its derivatives are the most widely-used evaporated ETLs in n-i-p and p-i-n type PSCs. Early in 2016, Bolink and his group evaporated 10 nm C_{60} and 40 nm C_{60}-PhIm double layer as ETL for enhancing conductivity and achieving good band alignment (Figure 4b)[57]. They deposited 10 nm N4,N4,N4″,N4‴-tetra([1,1′-biphenyl]-4-yl)-[1,1′:4′,1″-terphenyl]-4,4″-diamine (TaTm) and 40 nm TaTm: F$_6$-TCNNQ as double-layer HTL and achieved a PCE of 16.5% on p-i-n devices. Later in 2018, the same team observed the reduction in leakage current and interfacial recombination via evaporating a 10 nm C_{60} interlayer on TiO$_2$ ETL, and obtained a PCE of 20.8%[58]. Numerous organic charge transport materials suitable for thermal evaporation illustrate the feasibility and extensibility of thermal evaporation technique in ETL/HTL deposition.

2 Chemical vapor deposition

Unlike thermal evaporation, CVD takes advantage of gas-state precursors to deposit perovskite layers through chemical

reactions[3]. CVD is usually performed in a tube furnace divided into high temperature region for material sublimation, and low temperature region for precursor deposition. Carrier gas such as dry N_2 flows into the tube furnace under precise control. CVD has attracted increasing attention because of its large-area film homogeneity. In 2014, Leyden et al. first introduced hybrid chemical vapor deposition (HCVD) to deposit ammonium salt[59]. They deposited MAI by CVD on thermally evaporated or spin-coated PbI_2 film in a tube furnace and found that the PSC performance was heavily affected by several experimental parameters including chamber pressure, carrier gas flow rate, material temperature and substrate temperature. They achieved a PCE of 11.8% with good stability. Recently, they optimized the method and improved the up-scalability of HCVD[60]. They demonstrated that the sputtered SnO_2 electron transport layer could be damaged during the HCVD process, so they deposited a thin layer of C_{60} at the interface of SnO_2 for protection and fabricated $Cs_{0.1}FA_{0.9}PbI_{2.9}Br_{0.1}$ perovskite film with good thermal stability. They achieved a PCE over 10% for a perovskite solar module with an area of 91.8 cm². Zhang and her group deposited organic salts organic salts via CVD on thermally coevaporated $PbI_{2-x}Cl_x$ templates[61]. They achieved a PCE of 18.1% with a device structure of ITO/Spiro-TTB/Perovskite/PCBM/BCP/Al. In addition, they found that the CVD-deposited perovskite films have good uniformity and crystallinity on textured silicon substrate, demonstrating the potential in the fabrication of tandem solar cells.

CVD is a promising vacuum deposition protocol for large-scale PSC module. Nevertheless, most of the reported literature focused on the CVD process of ammonium salt, while the lead halide layer was deposited through either vacuum deposition or solution processing. Qi and his group used raster ultrasonic spray coating (RUS) method to deposit lead halide template, followed by depositing FAI, FABr and MACl via CVD[62]. They claimed that this method overcomes the coating size limitation of the existing spin-coating method or stationary spray method with negligible loss of lead waste. Using this method, they achieved a PCE of 14.7% with an active area of 12.0 cm². A few aspects of the CVD method still need further optimizations. Firstly, it will be beneficial to further improve the cost-effectiveness of the CVD method. Secondly, it will be desirable to develop an effective way to clean the remaining precursor materials adsorbed on the furnace from the previous CVD runs to improve reproducibility. Thirdly, to achieve scalable fabrication of CVD-processed perovskite solar module, it is important to better understand the effect of numerous parameters (e.g., pressure in the tube furnace, gas flow rate, heating temperature, temperature increasing rate, etc.) on the CVD-based perovskite solar cell device performance[63].

3   Atomic layer deposition

Although perovskite layers with good uniformity can be deposited by thermal evaporation, it still has several drawbacks. Firstly, it is not suitable for depositing materials with high sublimation temperatures. Some commonly-used metal oxides in PSCs such as TiO_2, SnO_2, NiO_x and Al_2O_3 exhibit sublimation temperatures above 1800 °C and are difficult to sublime by ordinary evaporation sources[64]. The excessive temperature of the evaporation source may deteriorate the PSC if the metal oxide is directly deposited on it. Secondly, thermal evaporation is not suitable for depositing ultra-thin layers with sub-nanometer control. ETLs for n-i-p PSCs require minor thickness for reducing serial resistance and full coverage without pinholes or cracks for reducing shunt leakage[47].

Nevertheless, the thermally evaporated molecules may nucleate directly and grow to islands in the case of Volmer–Weber mode and cannot meet the strict requirement for high-quality ultra-thin CTLs or encapsulants[7]. Therefore, it is imperative to develop a better vacuum deposition technique to fabricate high-quality metal oxides layers for efficient PSCs.

ALD is a self-limiting vapor deposition method, which comprises of a binary sequence of successive, self-terminating and irreversible vapor-solid chemical reactions[65]. For the first half-reaction of ALD, a gaseous precursor is chemisorbed onto the substrate and afterwards byproducts and unreacted precursor are purged out of the vacuum chamber. For the next half-reaction, the second gaseous precursor is pulsed into the chamber and bonded to the surface reaction sites. Afterwards, byproducts and precursors are purged out of the reactor and a new cycle begins. The cycles can be repeated until a thin film with a desired thickness is obtained (Figure 5a). The self-limiting nature of ALD gives rise to a precise control of film thickness at atomic scale, highly conformal film growth, and high crystallinity which is independent of the substrate structure. However, ALD gives a much smaller deposition rate compared with thermal evaporation with higher fabrication cost. ALD has proven it useful for synthesis of several key components in PSCs including ETLs, HTLs, and encapsulants, which are crucial for the performance and stability of PSCs.

3.1   ALD for CTLs

ALD can fabricate ultra-thin CTLs with conformal and compact film growth, which is favorable for improving device performance. In addition, the compact CTL film produced by ALD can also inhibit the penetration of water and oxygen molecules and thereby improve the environmental stability of devices[66]. Lv et al. reported a low-temperature ALD technique to deposit pinhole-free TiO_2 as ETL in p-i-n PSCs with a structure of ITO/NiO_x/perovskite/$PC_{61}BM$/TiO_2/Ag and achieved a PCE of 18.3% (Figure 5b)[67]. They demonstrated that the ALD process has negligible damage to the underlying perovskite layer. In addition, the compact ALD-TiO_2 layer can not only extract photogenerated holes, but can also reduce interfacial nonradiative recombination and resist water penetration, which is evident by the long-term humidity stability test, demonstrating the feasibility and superiority of ALD technique.

Although high efficiencies have been achieved for TiO_2-based PSCs, TiO_2 can serve as a catalyst for the decomposition of perovskite under ultraviolet light illumination, posing a major obstacle for industrial application[68,69]. Therefore, chemically stable and outperforming ETLs are highly desirable. SnO_2 is another widely used ETL because of its high optical transmission, high carrier mobility, chemical stability, and good band alignment with perovskites and can be deposited using ALD technique[68,70]. In 2015, Correa Baena et al. firstly used ALD to deposit SnO_2 as ETL with a processing temperature of 118 °C (Figures 5c and 5d)[71]. They compared the ALD processed TiO_2 with SnO_2 and found better efficiency, reduced hysteresis and improved efficiency can be achieved with ALD-SnO_2 based devices. A PCE of 18.4% was achieved with a V_{oc} up to 1.19 V. Later in 2017, the same team reached a PCE over 20% with a relatively high V_{oc} of 1.23 V (Figure 5e)[72]. Wang et al. reported a plasma-enhanced ALD (Pe-ALD) technique to lower the deposition temperature of SnO_2 to below 100 °C without sacrificing the efficiency[73], which is suitable for fabricating perovskite-silicon monolithic tandem cells or p-i-n PSCs to avoid the perovskite decomposition concerns under high temperature.

NiO_x is an ideal inorganic HTM for PSCs because of the chemical
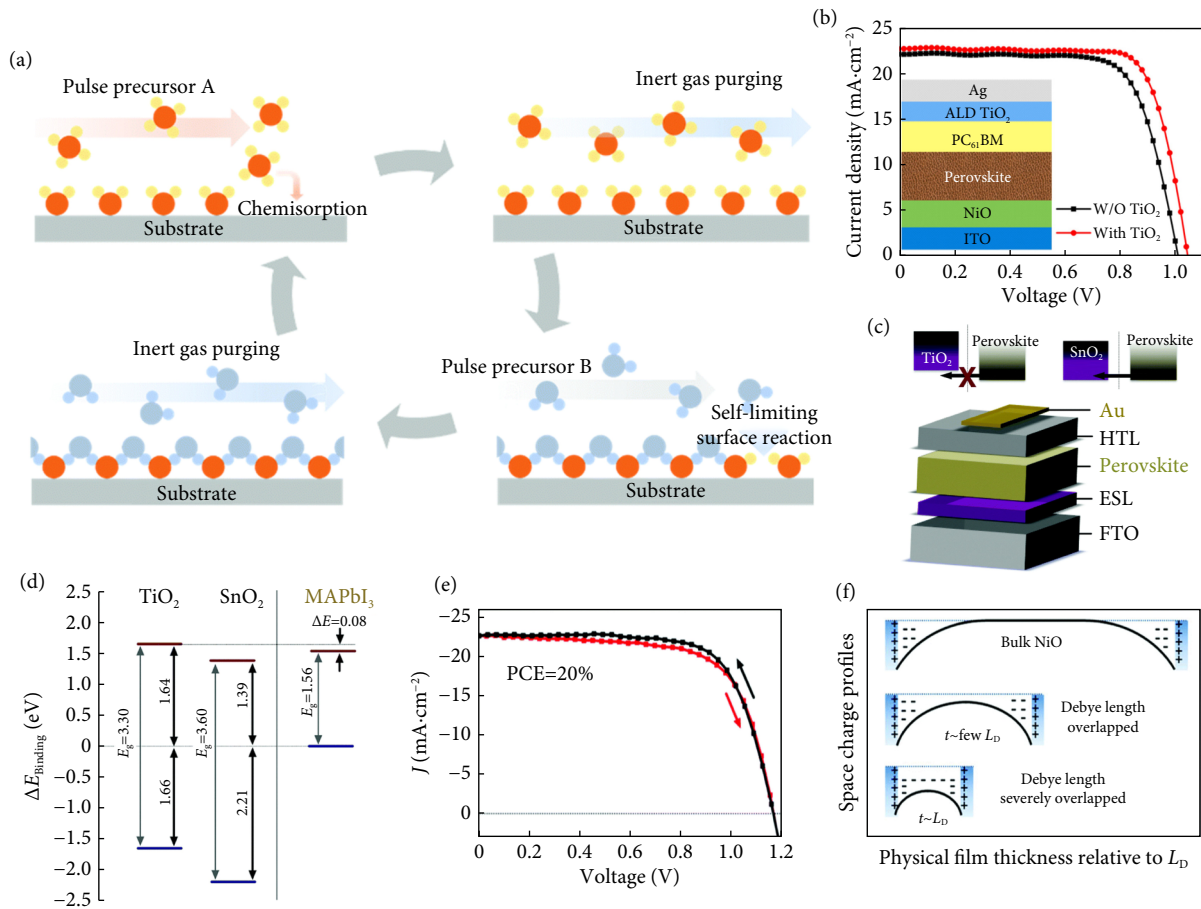
Fig. 5   ALD for CTLs. (a) Schematic illustration of the ALD process (reprinted with permission from ref. [45], © 2019 The Royal Society of Chemistry). **(b)** Device structure and J–V curve of PSC using ALD-TiO$_2$ as ETL (reprinted with permission from ref. [65], © 2018 American Chemical Society). **(c** and **d)** Schematic conduction band diagram of the perovskite films and the electron selective layers, TiO$_2$ and SnO$_2$ for MAPbI$_3$ PSCs (reprinted with permission from ref. [69], © 2015 The Royal Society of Chemistry). **(e)** Current-voltage characteristics of the PSC using ALD-SnO$_2$ as ETL (reprinted with permission from ref. [70], © 2017 The Royal Society of Chemistry). **(f)** Schematic images of physical film thickness relative to the Debye length versus space charge profiles (reprinted with permission from ref. [72], © 2016 The Royal Society of Chemistry).

stability and appropriate valence band alignment with perovskites. Nevertheless, because of the high bonding strengths within NiO$_x$ crystals, NiO$_x$ thicker than a few nanometers showed significantly reduced hole conductivity[74]. ALD can be a suitable deposition method for NiO$_x$ thin layer. Seo et al. optimized the ALD thickness of NiO to fabricate efficient PSCs (Figure 5f)[74]. They found that an ultra-thin NiO film (5 nm) comparable with the Debye length (1–2 nm) showed higher hole conductivity by overlapping space charge regions and sufficient electron blocking capability. A PCE of 16.4% was obtained with a device structure of FTO/NiO/MAPbI$_3$/PCBM/Ag.

3.2   ALD for tandem solar cells

Typically, a monolithic tandem solar cell comprises of a semi-transparent wide-bandgap top-cell, a narrow-bandgap bottom cell, and interconnecting layers[75]. Near-infrared light needs to pass through the top-cell and be absorbed by the bottom cell, which requires that the front electrode of the top cell and interconnecting layer are highly transmissive. Sputtered transparent conducting oxides (TCOs) were frequently used as transparent electrodes for top cells but the high molecular kinetic energy by sputtering may deteriorate the underlying perovskite film[76]. A buffer layer should be employed to protect the sensitive perovskite layer. Considering the low thermal tolerance of the underlying perovskite, ALD is an

ideal method for depositing the buffer layer between the CTL and transparent electrode[65]. The most commonly-used ALD buffer layer is SnO$_2$ for top cells with a p-i-n structure, which can facilitate the charge transport and inhibit water penetration to improve stability without sacrificing the light transmittance[44,45]. To date, many reported efficient monolithic Si-perovskite tandem cells deposit an ALD-SnO$_2$ thin layer between the sputtered TCO and C$_{60}$, and by now the efficiency has reached 31.25%[2].

Apart from buffer layers, ALD can also be employed to deposit tunnel junctions serving as substitutes for sputtered TCOs. The commonly-used thick TCOs exhibit high parasitic absorption of visible and near-infrared light, which is not favorable for the efficiency of bottom-cells. Moore et al. reported a conformal, low-conductivity AZO layer by ALD to fabricate flexible all-perovskite tandem solar cells[77]. The ALD-grown AZO tunnel junction is compact and water resistant which can reduce shunting as well as degradation from spin-coating on top of the bottom perovskite cell. They achieved PCEs of 23.1% and 21.3% on rigid and flexible plastic substrates.

3.3   ALD for encapsulants

In order for PSCs to become a reliable photovoltaic technology for commercialization, stable operations under a variety of environmental conditions for several years or even decades are required[78].

The key factor in achieving PSCs with good stability is developing stable perovskite absorbers and device structures including encapsulation, which can isolate underlying functional layers from stressors in the environment, including moisture and oxygen[47]. ALD is a powerful tool for depositing thin-film encapsulants which consists of a dense inorganic layer or a nanolaminate of inorganic and organic layers to achieve a low water vapor transmission rate (WVTR)[66]. In 2018, Choi et al. employed ALD to deposit a 50 nm Al_2O_3 layer at 95 °C as an encapsulant and achieved a WVTR of 1.84×10^{-2} $g \cdot m^{-2} \cdot d^{-1}$[79]. They fabricated devices with the structure of FTO/c-TiO_2/m-TiO_2/Perovskite/HTM/Al_2O_3 and achieved less than 4% decrease in PCE after 7500 hours of exposure to 50% relative humidity (RH) (Figure 6d). Later Ramos et al. highlighted the importance of ALD-Al_2O_3 temperature on the PSC performance (Figures 6a and 6b)[80]. They compared the efficiency of PSCs with the ALD-Al_2O_3 encapsulation process at 60 °C and 90 °C, and found devices with ALD-Al_2O_3 at 60 °C exhibited much higher J_{sc}, V_{oc} and FF and can retain 93.6% of the original PCE after encapsulation. Integrating inorganic thin layers with organic layers is an effective strategy to encapsulate PSCs where the insertion of organic layers can effectively elongate the tortuous path of the penetrating moisture and oxygen vapors and enhance the flexibility of the encapsulant by releasing the residual stress. Lee et al. reported an organic/inorganic multilayer encapsulation technique which consist of ALD-Al_2O_3 and pV3D3 layers (Figure 6c)[81]. They found the direct deposition of multilayer encapsulants onto the PSC causes negligible efficiency decline and achieved a WVTR on the order of 10^{-4} $g \cdot m^{-2} \cdot d^{-1}$.

4 Magnetron sputtering

Magnetron sputtering is a physical vapor deposition process where positive argon ions from the plasma collide with the negatively based target material, which causes target atoms to escape from the target surface and deposit onto the substrate. Strong magnetic fields are used to confine particles near the target surface during magnetron sputtering, which increases the ion density and contributes to a high sputtering rate. Magnetron sputtering have the advantages of high deposition rate, thorough coverage of materials, uniformity over large-area substrates, and highly adhesive
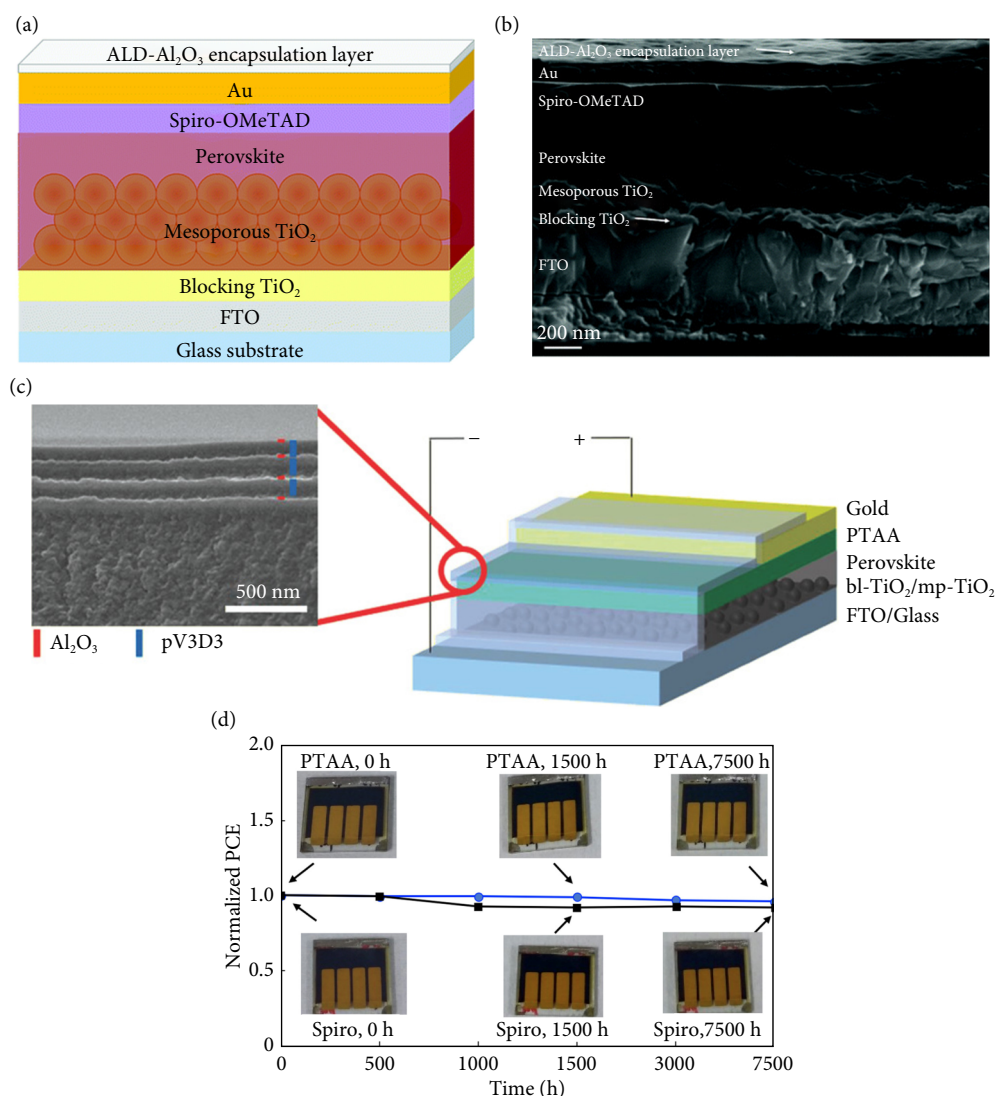

Fig. 6   ALD for thin-film encapsulation. (**a** and **b**) Schematic and cross-sectional SEM images of PSCs with the ALD–Al_2O_3 encapsulation layer (reprinted with permission from ref. [78], © 2018 The Royal Society of Chemistry). (**c**) Schematic illustration of the encapsulated PSC and the cross-sectional SEM image of the composite encapsulation (reprinted with permission from ref. [79], © 2017 Wiley VCH). (**d**) Long-term stability of PSCs with 50 nm Al_2O_3 as encapsulation. The PSCs were stored at room temperature (dark) in 50% RH for 7500 h (reprinted with permission from ref. [77], © 2018 Elsevier Inc).

coating of substrates. One of the disadvantages of magnetron sputtering is that the high kinetic energy of the sputtered particles may damage sensitive functional layers beneath. Magnetron sputtering can be available in depositing CTLs, transparent electrode, and perovskite absorbers in the field of PSCs.

4.1   Magnetron sputtering for CTLs

NiO_x is a commonly used HTL for inverted PSCs and can be deposited using magnetron sputtering. The first route is to sputter metallic nickel film followed by oxidizing to NiO_x, but it cannot guarantee full conversion and rarely used in fabricating PSCs. Another route is to conduct the magnetron sputtering in an oxygen atmosphere and the sputtered Ni atoms can react with oxygen to form NiO_x onto the substrate. The properties of the sputtered NiO_x can be affected by several factors including sputtering power, sputtering thickness, Ar/O_2 gas ratio, substrate temperature and post-annealing treatment[82]. The sputtered NiO_x usually exhibited a preferred orientation, which is closely related to the sputtering conditions within the chamber. Sputtered NiO_x as HTL has been reported previously but the reported PCEs were usually low because of the poor fill factor and small short current density, which is largely attributed to the poor conductivity of sputtered NiO_x[83]. In order to address this issue, dopants such as Mg were incorporated into the sputtered NiO_x film to enhance the conductivity. Li et al. reported a sputtered $NiMgO_x$ film by cosputtering metallic nickel target and MgO target[83]. They found that by introducing MgO doping and performing the sputtering at a low oxygen partial pressure, the deposited $NiMgO_x$ film exhibits better transmittance and conductivity. In addition, the $NiMgO_x$ had a better energy band alignment and pronounced PL quenching (Figure 7a), which is critical to reducing potential loss during hole injection. They achieved a PCE of 18.5% with a device structure of ITO /$NiMgO_x$/$MAPbI_3$/PCBM/ZnMgO/Al (Figure 7b).

SnO_2 ETL can also be deposited by magnetron sputtering. Similar to NiO_x, various parameters during sputtering can affect the property of SnO_2 film[68]. In 2019, Bai et al. investigated two types of SnO_2 targets sputtered by RF and DC supplies and found the devices based on RF-sputtered target had better performance (Figure 7c)[84]. They also found that the gas ratio of Ar/O_2 during sputtering process has a great impact on the stoichiometry, crystallinity and morphology of sputtered SnO_2 film (Figure 7d). They achieved a PCE of 18.20% and 14.71% in small area devices and 16.07 cm² modules, respectively. Later Qiu et al. demonstrated that a highly oxidizing environment is critical to obtain high-quality sputtered SnO_2 films (Figure 7e)[85]. They optimized the sputtering parameters and achieved a PCE of 20.2% and a T_{80} operational lifetime of 625 hours, which is the highest one using sputtered SnO_2 as ETL (Figure 7f).

4.2   Magnetron sputtering for transparent electrodes

Transparent conductive oxides (TCOs) such as indium zinc oxide (IZO), indium tin oxide (ITO), aluminum doped zinc oxide (AZO), and fluorine doped tin oxide (FTO) can be used as transparent electrodes for semitransparent PSCs and monolithic tandem solar cells (Figure 7g). Magnetron sputtering has been widely used in depositing TCOs on top of perovskite layers with good transmittance and conductivity. Nevertheless, the large kinetic energy of sputtered atoms may damage the underlying functional layers and thus deteriorate the device[86]. Therefore, a buffer layer is needed before sputtering TCO. Zhu et al. employed thermally evaporated MoO_x to prevent the sputtering damage of ITO owing to its low parasitic absorption and good compatibility to ensure

contact (Figure 7h)[76]. They found a trade-off between the sputtering power and the thickness of buffer layer. They achieved a PCE of 18% for perovskite/SHJ monolithic tandem cells with the optimized sputtering power of 40 W and 9 nm MoO_x. In 2020, Lim et al. reported a two-step linear facing target sputtering method to deposit InZnSnO (IZTO) electrode (Figure 7i)[87]. They sputtered a thin IZTO layer as a buffer followed by sputtering a thick dense IZTO layer. They demonstrated that their method can produce transparent electrodes without any plasma damage. Watson et al. introduced a structure of MoO_x/ITO/Ag/ITO (MoO_x/IAI) with high average transmittance as the top transparent electrode[88]. The 12 nm-thick Ag intermediate layer can enhance the conductivity and 50 nm-thick ITO layers guarantee high transmittance in the wavelength range from 300–1300 nm. In addition, this composite electrode can serve as an effective barrier to oxygen and moisture and improve environmental stability.

4.3   Magnetron sputtering for perovskite absorbers

Magnetron sputtering has the advantage to deposit large-area uniform coating and can be a suitable candidate for depositing perovskite absorbers. Gao et al. demonstrated that uniform and dense perovskite films can be deposited by magnetron sputtering in a few minutes (Figures 7j and 7i)[89] . They mechanosynthesized $MAPbI_3$ perovskite powder and pressed it into a specific shape to fabricate the $MAPbI_3$ target. Afterwards the target was sputtered to fabricate perovskite thin films. They further introduced Cl into the perovskite and combined with MAI post-treatment, they achieved a champion PCE of 15.52% for magnetron sputtered $MAPbI_3$ PSCs. Later in 2022, a PCE of 17.10% was obtained by the same team[90]. Large-area $CsPbBr_3$ perovskite films were also reported by one-step RF sputtering[91].

5   Pulsed laser deposition

Pulsed laser deposition is a PVD method where a high-energy laser is focused on the target material. The absorption of the laser energy causes electron excitations, which can convert to thermal and chemical energies and sublime the target material[92]. The PLD process can be divided into four steps: (1) Laser absorption and laser-target interaction. (2) Plasma plume formation. (3) Material deposition. (4) Nucleation and growth. The mechanism of PLD is complex as a variety of energetic particles including charge-free particles, atoms, ions, electrons form a plasma plume and deposit onto the substrate[64]. PLD has several advantages making it competitive for film deposition[93]. Firstly, only a few parameters related to laser need to be controlled such as laser pulse energy and laser repetition rate, making the deposition process feasible. Secondly, the stoichiometry of material can be preserved. The deposited film usually has similar stoichiometry as the raw material. Besides, the film thickness can be well-controlled to atomic monolayer by manipulating the number of pulses. In addition, a smaller target is required compared with magnetron sputtering. While there exist several limitations of PLD which may restrict its application in PSC fabrication[92]. The plasma plume exhibits a narrow angular distribution, posing an obstacle for the large-area film deposition. Micrometer-sized particles may splash onto the substrate because of the sub-surface boiling, expulsion of the liquid layer, and exfoliation of the target, which may have a detrimental effect to the underlying layers.

5.1   PLD for transparent electrodes

Sputtered conducting metal oxides were widely accepted as transparent electrodes for the fabrication of semitransparent PSCs. While the high kinetic energy of sputtered particles can damage
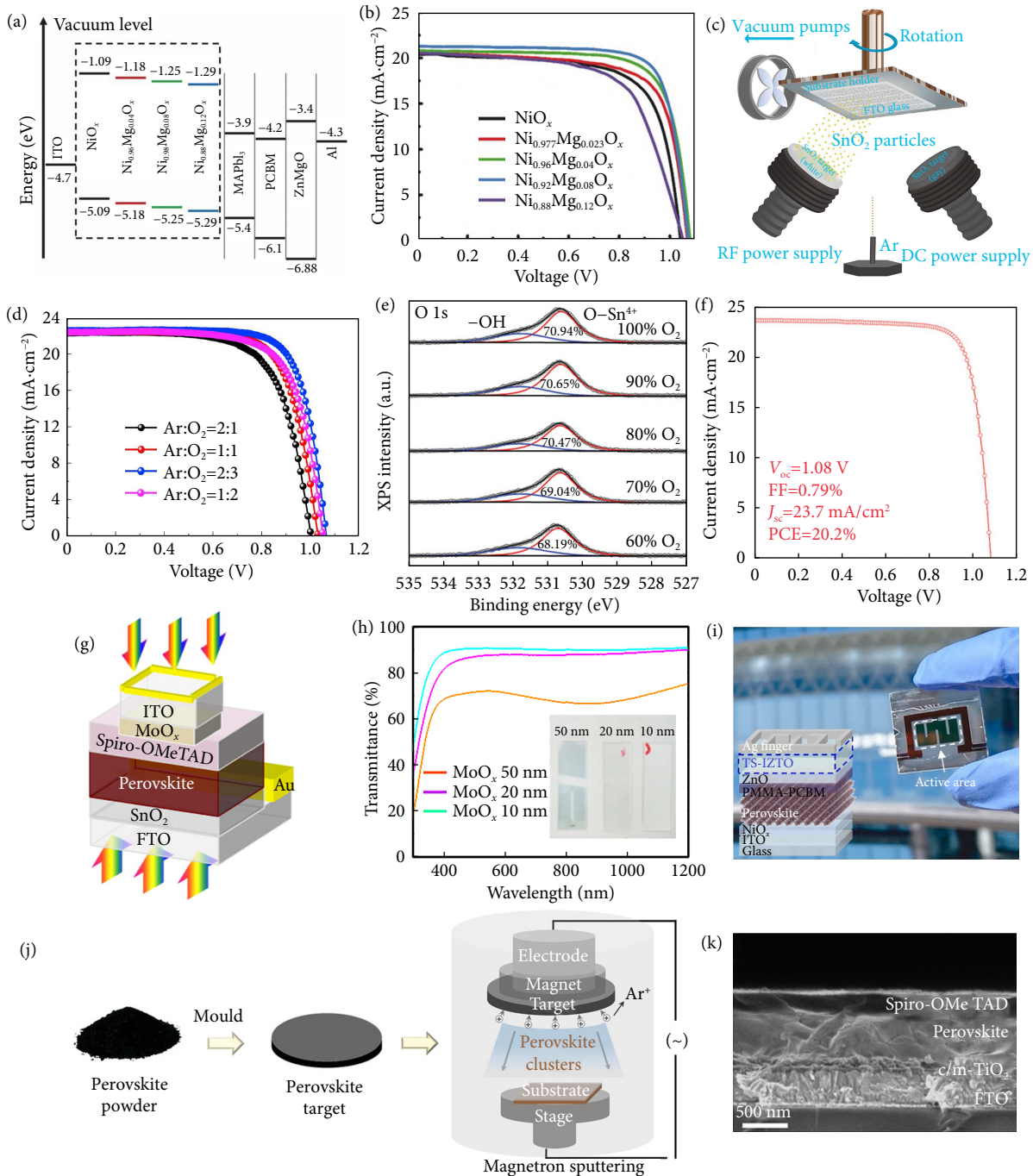
Fig. 7 Applications of magnetron sputtering for fabricating PSCs. (a and b) Energy band diagram **(a)** and current–voltage characteristics **(b)** of sputtered MgO doped NiO_x as ETL (reprinted with permission from ref. [81], © 2017 The Authors). **(c)** Schematic illustration of SnO_2 deposition process of DC/RF magnetron sputtering. **(d)** J–V curves of PSC based on sputtered SnO_2 film with different Ar/O_2 ratio. **(c and d)** Reprinted with permission from ref. [82], © 2019 International Solar Energy Society. **(e)** XPS O 1s core level of the SnO_2 films deposited with different oxygen ratio. **(f)** J–V curve of the champion device based on the sputtered SnO_2 ETL and $MAPbI_3$ perovskite film. **(e and f)** Reprinted with permission from ref. [83], © 2019 The Authors. **(g)** Schematic illustration of the semi-transparent PSC with two illumination direction. **(h)** Transmittance of different thicknesses of MoO_x buffer layers. **(g and h)** Reprinted with permission from ref. [74], © 2017 Elsevier Ltd. **(i)** Photograph and schematic device structure of semi-transparent PSC with ITO anode and IZTO top cathode (reprinted with permission from ref. [85], © 2020 Elsevier Ltd). **(j)** Scheme of the perovskite layer preparation process via sputtering. **(k)** Cross-sectional SEM image of PSCs produced via magnetron sputtering. **(j and k)** Reprinted with permission from ref. [87], © 2021 The Authors.

the sensitive underlying functional layers. Additionally, the difference in sputtering yield of multicompounds make the stoichiometry of deposited films unpredictable[64]. PLD is suitable for the depositing materials with high sublimation temperature and can preserve the stoichiometry independent of the volatility and evaporation pressures. Morales-Masis and her group used a large-area

PLD system to deposit wafer-scale (4 inch) amorphous Zr-doped In_2O_3 for the scalable fabrication of efficient semitransparent PSCs (Figure 8a)[64]. They found that a higher pressure during ablation enables deposition of Zr-doped In_2O_3 without damage to the sensitive layers beneath. They also compared sputtered TCO with PLD-processed TCO (Figure 8b) and found less parasitic absorp-
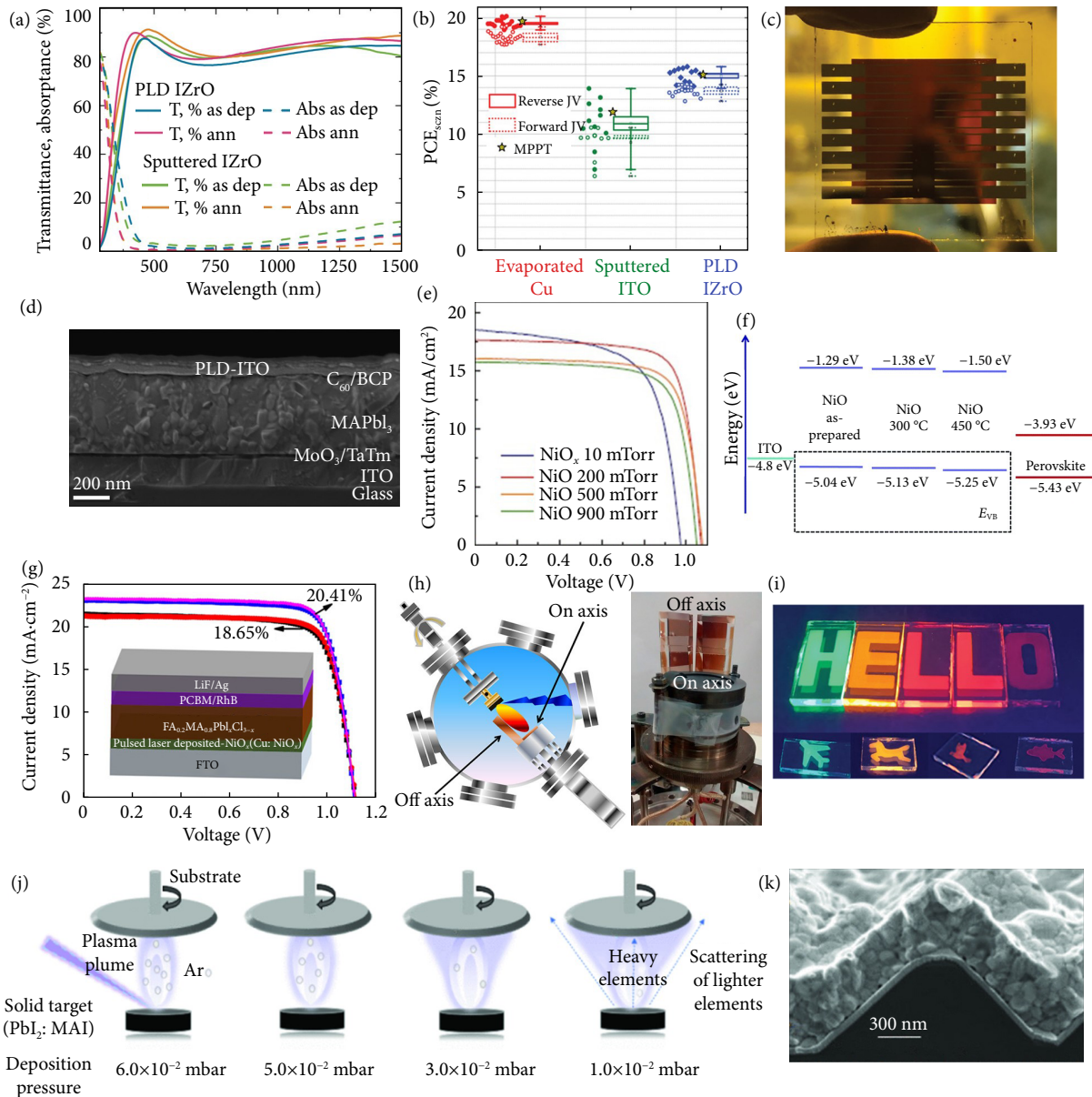
Fig. 8 Applications of PLD for fabricating PSCs. (**a** and **b**) Transmittance and absorptance spectrum of TCO films deposited by PLD and magnetron sputtering method, respectively (reprinted with permission from ref. [62], © 2021 The Authors). (**c** and **d**) Photograph (**c**) and cross-sectional SEM image (**d**) of the all-vacuum deposited semitransparent PSCs with ALD-grown ITO electrode (reprinted with permission from ref. [93], © 2022 The Authors). (**e**) *J–V* characteristics of PSCs based on PLD-grown NiO$_x$ films, deposited at different oxygen partial pressure (reprinted with permission from ref. [94], © 2015 Wiley VCH). (**f**) Energy band diagram of PLD-grown NiO at different annealing temperatures (reprinted with permission from ref. [95], © 2017 The Royal Society of Chemistry). (**g**) *J–V* curves of PSCs based on Cu doped NiO$_x$ and undoped NiO$_x$ HTLs and corresponding device structure (reprinted with permission from ref. [96], © 2020 American Chemical Society). (**h**) Schematic presentation and picture of the substrate arrangement for on-axis and off-axis PLD deposition (reproduced with permission from ref. [101], © 2015 American Chemical Society). (**i**) Photographs of CsPbI$_x$Br$_{1-x}$ films under the illumination of an ultraviolet fluorescent lamp (reprinted with permission from ref. [105], © 2021 Wiley-VCH). (**j**) Schematic illustration of the shape of plasma plume at different pressures. (**k**) Cross-sectional SEM image of the conformal growth of the PLD-grown perovskite film on textured Si substrate. (**J** and **k**) Reprinted with permission from ref. [103], © 2021 IEEE.

tion loss, higher crystallinity and preferential orientation was achieved for PLD-grown TCO, demonstrating the superiority of the method. They fabricated semitransparent PSCs and obtained a PCE of 15.1%. Later the same group studied the influence of vacuum pressure in the structural and optoelectronic properties of PLD-grown TCO[94]. They found the pressure can affect the sheet resistance, free carrier density, electron mobility, and light absorption coefficient of the deposited TCO film, thus influencing the performance of semitransparent PSCs. The increased pressure leads to an improved V_{oc} and fill factor. Bolink and his group further

optimized the deposition parameters such as chamber pressure and investigate its effect on transmittance and device performance[95]. Combined with thermally evaporated MAPbI$_3$ as perovskite absorber, C$_{60}$/BCP as ETL and TaTm as HTL, they achieved PCE more than 18% for semitransparent PSCs (Figures 8c and 8d).

5.2 PLD for CTLs

Metal oxides as charge transport layers can be deposited through PLD method. NiO$_x$ as a commonly-used HTL in p-i-n type PSCs

has been investigated by PLD approach. Early in 2015, Seok and his group reported PLD-grown nanostructured NiO film with good optical transparency (Figure 8e)[96]. They found that the transmittance and crystallinity of the NiO film can be affected by the oxygen partial pressure in the vacuum chamber. By optimizing the oxygen partial pressure and deposition thickness, they achieved a PCE of 17.3% with the device structure of ITO/NiO/MAPbI₃/PCBM/LiF/Al. Additionally, the fill factor reached as high as 81.3%, indicating a minor shunt resistance at the NiO/MAPbI₃ interface. Later Cao and his group reported that doping the ablated target with lithium (Li) can significantly enhance the conductivity of the PLD-grown NiO film[97]. They also found that post-annealing treatment at 450 °C contributed to a more uniform surface morphology, higher transmittance and enhanced in-plane crystal orientation (Figure 8f). They achieved a PCE of 15.51% using NiO:Li as HTL. Later in 2020, Feng at al. investigated the optoelectronic properties of Cu-doped NiO_x as HTL[98]. They demonstrated that Cu^+ as dopants can occupy the Ni vacancies, resulting in enhanced crystallinity and hole mobility. In addition, the NiO_x:Cu film exhibited higher conductivity and faster charge transport and extraction capability. Combined with solution-processed $FA_{0.2}MA_{0.8}PbI_xCl_{3-x}$ perovskite absorber they achieved a champion PCE of 20.41% (Figure 8g). PLD-processed metal oxides as ETLs such as TiO_2, Zn_2SO_4, $InGaSnO_4$ were also reported[99–101].

5.3 PLD for perovskite layers

The unique advantage of stoichiometry transfer from bulk material to thin film render it feasible for depositing perovskite layers with various components. While the organic components in perovskite are sensitive to excessive heat and may decompose under high laser energy, which indicates that the PLD-grown perovskite needs to be carefully controlled[102]. Early in 2015, Ogale and his group demonstrated that perovskite films composed of $MAPbI_xCl_{3-x}$ or $MASnI_3$ can be produced via PLD technique without any further annealing treatment[103]. They adopted off-axis deposition protocol to avoid ion-induced tiny clusters directly deposited onto the substrate (Figure 8h). They obtained a PCE of 7.7%. Later the same team optimized the molar ratio of lead halide and ammonium salt of the target and used Ar/H_2 mixed gas for momentum softening of the generated radical in the plasma plume[104]. The efficiency was further increased to 10.9%. They also reported PLD-grown perovskite with tunable bandgap from 1.6 to 2.3 eV. In 2021, Soto-Montero et al. addressed the importance of target composition and deposition parameters such as vacuum pressure, precursor ratio, to tune the microstructure and properties of ALD-grown $MAPbI_3$ films (Figure 8j)[105]. They also reported the conformal growth of PLD-processed perovskite on textured Si wafer (Figure 8k). Mitzi and his group adopted resonant infrared, matrix-assisted pulsed laser evaporation (RIR-MAPLE) to deposit $MAPbI_3$ perovskite films[102]. Instead of directly ablating the target, the laser was absorbed by the cryogenically frozen solvent matrix and resonant with the specific chemical bond in the solvent, which carries the material to the substrate. Compared with conventional PLD method, RIR-MAPLE can eliminate the risk of damaging laser-sensitive organic components. Adopting this strategy, they obtained a PCE more than 12%.

Compared with MA-containing perovskite, Cs-based inorganic perovskite absorbers do not contain organic components and are more suitable for PLD growth. Xu and his group applied PLD to deposit $CsPbBr_3$ film on mesoporous TiO_2 (m-TiO_2) substrate[106]. They found that PLD-grown $CsPbBr_3$ can permeate into the m-

TiO_2 layer with uniform distribution. They obtained a champion PCE of 6.32% with a V_{oc} of 1.37 V. Later the same team developed a two-step successive PLD deposition approach to fabricate inorganic perovskite layers with tunable bandgap (Figure 8i)[107]. They deposited $CsPbBr_3$, $CsPbIBr_2$, $CsPbI_2Br$ and $CsPbI_3$ and proved their good stability under high humidity (90%–95%). Sn-based perovskites such as γ-$CsSnI_3$, $Cs_2AgBiBr_6$, $MASnI_3$ were also reported to be fabricated via PLD method[108–110].

6 Electron beam evaporation

Compared with PLD using high-energy laser to sublime the material, e-beam evaporation employs intense electron beam to provide sufficient energy for evaporating materials. E-beam evaporation is suitable for depositing metal oxides such as TiO_2, SnO_2, NiO_x, Nb_2O_5 which usually exhibit high sublime temperatures[111]. Inorganic perovskite such as $CsPbBr_3$ can also be deposited by this method[112]. In 2015, Cheyns and his group employed e-beam evaporation to deposit compact TiO_2- as ETL[113]. They found that TiO_2 can be deposited onto the substrate below 77 °C, indicating that e-beam evaporated TiO_2 was applicable to flexible plastic substrates. By optimizing the TiO_2 thickness, they obtained PCEs of 14.6% and 13.5% on rigid and flexible substrates, respectively. Sharp et al. found that TiO_2 films evaporated in an oxygen-deficient environment exhibited natural hole traps[114]. The deep-level hole traps in ETL contributed to higher photoconductivity and reduced photocatalytic activity, which benefits the device efficiency and operational stability. A champion efficiency of 19.0% was achieved. Fang et al. employed e-beam evaporation to deposit SnO_2 and achieved a PCE of 18.2%[115]. Later Lidzey and his team used similar strategy and achieved a PCE of 19.3%[116]. Nb_2O_5 was also reported as a suitable ETL candidate for PSCs because of its good conduction band alignment with perovskite and high carrier mobility[117]. Liu et al. used e-beam evaporation to deposit Nb_2O_5 as ETL without any further post-treatment. They optimized the deposition thickness and found that PSCs with 60 nm thick ETL delivered the highest PCE of 18.59%[117]. They also demonstrated that e-beam evaporated Nb_2O_5 is advantageous for the fabrication of large-area flexible PSCs.

NiO_x as a widely-used HTL was extensively investigated by e-beam evaporation[118]. Paetzold and his group studied oxygen partial pressure and its impact on the parasitic light absorption of e-beam evaporated NiO_x[119]. As the oxygen pressure increased, the absorptance of NiO_x films decreased significantly over the entire wavelength range. It was attributed to a change of the oxidation state change of nickel ions. They achieved a PCE of 15.4% for all-vacuum deposited PSCs with a device structure of ITO/NiO_x/MAPbI₃/C_{60}/BCP/Au. They also obtained a PCE of 18.5% based on inkjet-printed perovskite and e-beam evaporated NiO_x HTL. Liu et al. proposed a device structure comprising e-beam evaporated NiO_x as HTL and Nb_2O_5 as ETL[120]. They demonstrated a good energy band alignment of the structure and achieved a PCE of 19.5%. Later the same team employed dual-source e-beam coevaporation to improve the device performance[121]. They deposited Cu doped NiO_x (Cu:NiO_x) and tungsten (W) doped Nb_2O_5 (W:Nb_2O_5) to improve the conductivity and tune the energy band of CTLs. In addition, they deposited a thin layer of titanium (Ti) between ETL and Ag electrode to prevent halide migration. They achieved PCEs of 21.32% and 19.01% with aperture areas of 0.1 and 1 cm², respectively. Recently, Liu et al. reported a surface redox engineering (SRE) strategy for e-beam evaporated NiO_x HTL[122]. They used Ar plasma treatment in vacuum followed

by dilute nitric acid to treat NiO_x substrates. They demonstrated that the SRE strategy can foster the formation of a stabilized NiO_x surface with enhanced conductivity, better energy band alignment with perovskite layer, and increased surface energy, which can improve the perovskite stacking mode on NiO_x layer. They obtained PCEs of 23.4%, 21.3%, 18.6% for small-area rigid devices, flexible devices and 156×156 mm² PSC modules, respectively.

7　Conclusions

In this review, we mainly focused on several vapor deposition methods including thermal evaporation, chemical vapor deposition, atomic layer deposition, pulsed laser deposition, magnetron sputtering, electron beam evaporation, and their applications in fabricating PSCs. The large-area homogeneity and industrial compatibility make them promising methods for scalable fabrication of PSC in the emerging solar PV markets. Thermal evaporation is a powerful tool for depositing perovskite layers which can be divided into dual-source evaporation, sequential evaporation, single-source evaporation, and vapor-solution hybrid method. ALD, PLD and e-beam evaporation are suitable for depositing inorganic CTLs such as TiO_2, SnO_2 and NiO_x. Thin-film encapsulants such as Al_2O_3 can be deposited by ALD technique. Magnetron sputtering can be used to deposit CTLs such as SnO_2 and NiO_x and transparent electrodes like TCOs. ALD and magnetron sputtering can also be applied in fabricating buffer layers and tunnel junction layers for monolithic tandem solar cells. Schematic illustrations of all-vacuum deposited PSCs are shown in Figure 9. Going forward, we foresee that vapor deposition methods will continue contributing to fabricating efficient and stable PSCs.
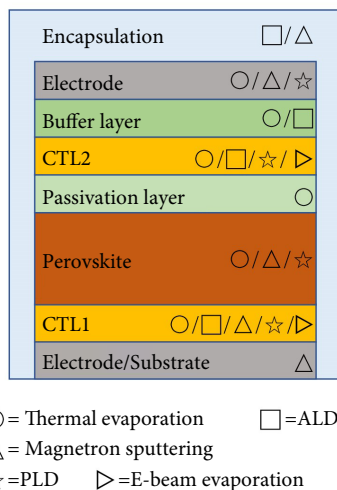

Fig. 9　Schematic illustrations of fully-vacuum deposited PSCs.

Acknowledgements

Article history

Additional information

Declaration of competing interest

The authors have no competing interests to declare that are relevant to the content of this article.

References

[1]　Lin, D. X., Zhan, Z. Y., Huang, X. L., Liu, P. Y., Xie, W. G. (2022). Advances in components engineering in vapor deposited perovskite thin film for photovoltaic application. *Materials Today Advances*, 16: 100277.

[2]　National Renewable Energy Laboratory. Best research-cell efficiency chart. Available at https://www.nrel.gov/pv/cell-efficiency. html.

[3]　Jiang, Y., He, S. S., Qiu, L. B., Zhao, Y. X., Qi, Y. B. (2022). Perovskite solar cells by vapor deposition based and assisted methods. *Applied Physics Reviews*, 9: 021305.

[4]　Li, H., Zhou, J., Tan, L., Li, M., Jiang, C., Wang, S., Zhao, X., Liu, Y., Zhang, Y., Ye, Y., et al. (2022). Sequential vacuum-evaporated perovskite solar cells with more than 24% efficiency. *Science Advances*, 8: eabo7422.

[5]　Wang, S. H., Li, X. T., Wu, J. B., Wen, W. J., Qi, Y. B. (2018). Fabrication of efficient metal halide perovskite solar cells by vacuum thermal evaporation: A progress review. *Current Opinion in Electrochemistry*, 11: 130–140.

[6]　Gil-Escrig, L., Roß, M., Sutter, J., Al-Ashouri, A., Becker, C., Albrecht, S. (2021). Fully vacuum-processed perovskite solar cells on pyramidal microtextures. *Solar RRL*, 5: 2000553.

[7]　Du, P. P., Wang, L., Li, J. H., Luo, J. J., Ma, Y., Tang, J., Zhai, T. Y. (2022). Thermal evaporation for halide perovskite optoelectronics: Fundamentals, progress, and outlook. *Advanced Optical Materials*, 10: 2101770.

[8]　Du, P. P., Li, J. H., Wang, L., Sun, L., Wang, X., Xu, X., Yang, L. B., Pang, J. C., Liang, W. X., Luo, J. J., et al. (2021). Efficient and large-area all vacuum-deposited perovskite light-emitting diodes via spatial confinement. *Nature Communications*, 12: 4751.

[9]　Li, Z. Z., Zhou, F. G., Yao, H. H., Ci, Z. P., Yang, Z., Jin, Z. W. (2021). Halide perovskites for high-performance X-ray detector. *Materials Today*, 48: 155–175.

[10]　Fan, Y., Qin, H. L., Mi, B. X., Gao, Z. Q., Huang, W. (2014). Progress in the fabrication of Cu_2ZnSnS_4 thin film for solar cells. *Acta Chimica Sinica*, 72: 643.

[11]　Era, M., Hattori, T., Taira, T., Tsutsui, T. (1997). Self-organized growth of PbI-based layered perovskite quantum well by dual-source vapor deposition. *Chemistry of Materials*, 9: 8–10.

[12] Liu, M. Z., Johnston, M. B., Snaith, H. J. (2013). Efficient planar heterojunction perovskite solar cells by vapour deposition. *Nature*, 501: 395–398.

[13] Malinkiewicz, O., Yella, A., Lee, Y. H., Espallargas, G. M., Graetzel, M., Nazeeruddin, M. K., Bolink, H. J. (2014). Perovskite solar cells employing organic charge-transport layers. *Nature Photonics*, 8: 128–132.

[14] Malinkiewicz, O., Roldán-Carmona, C., Soriano, A., Bandiello, E., Camacho, L., Nazeeruddin, M. K., Bolink, H. J. (2014). Metal-oxide-free methylammonium lead iodide perovskite-based solar cells: The influence of organic charge transport layers. *Advanced Energy Materials*, 4: 1400345.

[15] Li, J., Wang, H., Chin, X. Y., Dewi, H. A., Vergeer, K., Goh, T. W., Lim, J. W. M., Lew, J. H., Loh, K. P., Soci, C., et al. (2020). Highly efficient thermally Co-evaporated perovskite solar cells and mini-modules. *Joule*, 4: 1035–1053.

[16] Dewi, H. A., Li, J., Wang, H., Chaudhary, B., Mathews, N., Mhaisalkar, S., Bruno, A. (2021). Excellent intrinsic long-term thermal stability of Co-evaporated MAPbI₃ solar cells at 85 °C. *Advanced Functional Materials*, 31: 2100557.

[17] Borchert, J., Levchuk, I., Snoek, L. C., Rothmann, M. U., Haver, R., Snaith, H. J., Brabec, C. J., Herz, L. M., Johnston, M. B. (2019). Impurity tracking enables enhanced control and reproducibility of hybrid perovskite vapor deposition. *ACS Applied Materials & Interfaces*, 11: 28851–28857.

[18] Borchert, J., Milot, R. L., Patel, J. B., Davies, C. L., Wright, A. D., Martínez Maestro, L., Snaith, H. J., Herz, L. M., Johnston, M. B. (2017). Large-area, highly uniform evaporated formamidinium lead triiodide thin films for solar cells. *ACS Energy Letters*, 2: 2799–2804.

[19] Lohmann, K. B., Motti, S. G., Oliver, R. D. J., Ramadan, A. J., Sansom, H. C., Yuan, Q., Elmestekawy, K. A., Patel, J. B., Ball, J. M., Herz, L. M., et al. (2022). Solvent-free method for defect reduction and improved performance of p-i-n vapor-deposited perovskite solar cells. *ACS Energy Lett*, 7: 1903–1911.

[20] Chiang, Y. H., Anaya, M., Stranks, S. D. (2020). Multisource vacuum deposition of methylammonium-free perovskite solar cells. *ACS Energy Letters*, 5: 2498–2504.

[21] Gil-Escrig, L., Dreessen, C., Kaya, I. C., Kim, B. S., Palazon, F., Sessolo, M., Bolink, H. J. (2020). Efficient vacuum-deposited perovskite solar cells with stable cubic FA$_{1-x}$MA$_x$PbI₃. *ACS Energy Letters*, 5: 3053–3061.

[22] Gil-Escrig, L., Dreessen, C., Palazon, F., Hawash, Z., Moons, E., Albrecht, S., Sessolo, M., Bolink, H. J. (2021). Efficient wide-bandgap mixed-cation and mixed-halide perovskite solar cells by vacuum deposition. *ACS Energy Letters*, 6: 827–836.

[23] Juarez-Perez, E. J., Ono, L. K., Qi, Y. B. (2019). Thermal degradation of formamidinium based lead halide perovskites into *sym*-triazine and hydrogen cyanide observed by coupled thermogravimetry-mass spectrometry analysis. *Journal of Materials Chemistry A*, 7: 16912–16919.

[24] Ball, J. M., Buizza, L., Sansom, H. C., Farrar, M. D., Klug, M. T., Borchert, J., Patel, J., Herz, L. M., Johnston, M. B., Snaith, H. J. (2019). Dual-source coevaporation of low-bandgap FA$_{1-x}$Cs$_x$Sn$_{1-y}$Pb$_y$I₃ perovskites for photovoltaics. *ACS Energy Letters*, 4: 2748–2756.

[25] Igual-Muñoz, A. M., Ávila, J., Boix, P. P., Bolink, H. J. (2020). FAPb₀.₅Sn₀.₅I₃: A narrow bandgap perovskite synthesized through evaporation methods for solar cell applications. *Solar RRL*, 4: 2070024.

[26] Lin, H. Y., Chen, C. Y., Hsu, B. W., Cheng, Y. L., Tsai, W. L., Huang, Y. C., Tsao, C. S., Lin, H. W. (2019). Efficient cesium lead halide perovskite solar cells through alternative thousand-layer rapid deposition. *Advanced Functional Materials*, 29: 1905163.

[27] Zhang, Z. B., Ji, R., Kroll, M., Hofstetter, Y. J., Jia, X. K., Becker-Koch, D., Paulus, F., Löffler, M., Nehm, F., Leo, K., et al. (2021). Efficient thermally evaporated γ-CsPbI₃ perovskite solar cells. *Advanced Energy Materials*, 11: 2100299.

[28] Antrack, T., Kroll, M., Sudzius, M., Cho, C., Imbrasas, P., Albaladejo-Siguan, M., Benduhn, J., Merten, L., Hinderhofer, A., Schreiber, F., et al. (2022). Optical properties of perovskite-organic multiple quantum wells. *Advanced Science*, 9: 2200379.

[29] Kroll, M., Dilara Ã−z, S., Zhang, Z. B., Ji, R., Schramm, T., Antrack, T., Vaynzof, Y., Olthof, S., Leo, K. (2022). Insights into the evaporation behaviour of FAI: Material degradation and consequences for perovskite solar cells. *Sustainable Energy & Fuels*, 6: 3230–3239.

[30] La-Placa, M. G., Guo, D. Y., Gil-Escrig, L., Palazon, F., Sessolo, M., Bolink, H. J. (2020). Dual-source vacuum deposition of pure and mixed halide 2D perovskites: Thin film characterization and processing guidelines. *Journal of Materials Chemistry C*, 8: 1902–1908.

[31] Lin, D. X., Gao, Y. J., Zhang, T. K., Zhan, Z. Y., Pang, N. N., Wu, Z. W., Chen, K., Shi, T. T., Pan, Z. Q., Liu, P. Y., et al. (2022). Vapor deposited pure α-FAPbI₃ perovskite solar cell via moisture-induced phase transition strategy. *Advanced Functional Materials*, 32: 2208392.

[32] Lee, J. H., Kim, B. S., Park, J., Lee, J. W., Kim, K. (2022). Opportunities and challenges for perovskite solar cells based on vacuum thermal evaporation. *Advanced Materials Technologies*, https://doi.org/10.1002/admt.202200928.

[33] Feng, J. S., Jiao, Y. X., Wang, H., Zhu, X. J., Sun, Y. M., Du, M. Y., Cao, Y. X., Yang, D., Liu, S. F. (2021). High-throughput large-area vacuum deposition for high-performance formamidine-based perovskite solar cells. *Energy & Environmental Science*, 14: 3035–3043.

[34] Choi, Y., Koo, D., Jeong, G., Kim, U., Kim, H., Huang, F. Z., Park, H. (2022). A vertically oriented two-dimensional Ruddlesden-Popper phase perovskite passivation layer for efficient and stable inverted perovskite solar cells. *Energy & Environmental Science*, 15: 3369–3378.

[35] Li, H., Tan, L., Jiang, C., Li, M., Zhou, J., Ye, Y., Liu, Y., Yi, C. (2022). Molten salt strategy for reproducible evaporation of efficient perovskite solar cells. *Advanced Functional Materials*, https://doi.org/10.1002/adfm.202211232.

[36] Ullah, S., Wang, J. M., Yang, P. X., Liu, L. L., Li, Y. Q., Rehman, A. U., Yang, S. E., Xia, T. Y., Guo, H. Z., Chen, Y. S. (2021). Evaporation deposition strategies for all-inorganic CsPb(I$_{1-x}$Br$_x$)₃ perovskite solar cells: Recent advances and perspectives. *Solar RRL*, 5: 2100172.

[37] Mitzi, D. B., Prikas, M. T., Chondroudis, K. (1999). Thin film deposition of organic−inorganic hybrid materials using a single source thermal ablation technique. *Chemistry of Materials*, 11: 542–544.

[38] Longo, G., Gil-Escrig, L., Degen, M. J., Sessolo, M., Bolink, H. J. (2015). Perovskite solar cells prepared by flash evaporation. *Chemical Communications* (*Cambridge, England*), 51: 7376–7378.

[39] El Ajjouri, Y., Palazon, F., Sessolo, M., Bolink, H. J. (2018). Single-source vacuum deposition of mechanosynthesized inorganic halide perovskites. *Chemistry of Materials*, 30: 7423–7427.

[40] Fan, P., Gu, D., Liang, G. X., Luo, J. T., Chen, J. L., Zheng, Z. H., Zhang, D. P. (2016). High-performance perovskite CH₃NH₃PbI₃ thin films for solar cells prepared by single-source physical vapour deposition. *Scientific Reports*, 6: 29910.

[41] Li, J., Gao, R. R., Gao, F., Lei, J., Wang, H. X., Wu, X., Li, J. B., Liu, H., Hua, X. D., Liu, S. Z. (2020). Fabrication of efficient CsPbBr₃ perovskite solar cells by single-source thermal evaporation. *Journal of Alloys and Compounds*, 818: 152903.

[42] Nasi, L., Calestani, D., Mezzadri, F., Mariano, F., Listorti, A., Ferro, P., Mazzeo, M., Mosca, R. (2020). All-inorganic CsPbBr₃ perovskite films prepared by single source thermal ablation. *Frontiers in Chemistry*, 8: 313.

[43] Klipfel, N., Haris, M. P. U., Kazim, S., Sutanto, A. A., Shibayama, N., Kanda, H., Asiri, A. M., Momblona, C., Ahmad, S., Nazeeruddin, M. K. (2022). Structural and photophysical investigation of single-source evaporation of CsFAPbI₃ and FAPbI₃ perovskite thin

films. *Journal of Materials Chemistry C*, 10: 10075–10082.

[44] Li, Y. C., Shi, B., Xu, Q. J., Yan, L. L., Ren, N. Y., Chen, Y. L., Han, W., Huang, Q., Zhao, Y., Zhang, X. D. (2021). Wide bandgap interface layer induced stabilized perovskite/silicon tandem solar cells with stability over ten thousand hours. *Advanced Energy Materials*, 11: 2102046.

[45] Mao, L., Yang, T., Zhang, H., Shi, J. H., Hu, Y. C., Zeng, P., Li, F. M., Gong, J., Fang, X. Y., Sun, Y. Q., et al. (2022). Fully textured, production-line compatible monolithic perovskite/silicon tandem solar cells approaching 29% efficiency. *Advanced Materials*, 34: 2206193.

[46] Wang, S. Y., Tan, L. G., Zhou, J. J., Li, M. H., Zhao, X., Li, H., Tress, W., Ding, L. M., Graetzel, M., Yi C. (2022). Over 24% efficient MA-free Cs$_x$FA$_{1−x}$PbX$_3$ perovskite solar cells. *Joule*, 6: 1344–1356.

[47] Seo, S., Jeong, S., Park, H., Shin, H., Park, N. G. (2019). Atomic layer deposition for efficient and stable perovskite solar cells. *Chemical Communications*, 55: 2403–2416.

[48] Polander, L. E., Pahner, P., Schwarze, M., Saalfrank, M., Koerner, C., Leo, K. (2014). Hole-transport material variation in fully vacuum deposited perovskite solar cells. *APL Materials*, 2: 081503.

[49] Cheng, Q. R., Chen, H. Y., Yang, F., Chen, Z. Y., Chen, W. J., Yang, H. Y., Shen, Y. X., Ou, X. M., Wu, Y. Y., Li, Y. W., et al. (2022). Molecular self-assembly regulated dopant-free hole transport materials for efficient and stable n-i-p perovskite solar cells and scalable modules. *Angewandte Chemie International Edition*, 61: e202210613.

[50] Du, G. Z., Yang, L., Zhang, C. P., Zhang, X. L., Rolston, N., Luo, Z. D., Zhang, J. B. (2022). Evaporated undoped spiro-OMeTAD enables stable perovskite solar cells exceeding 20% efficiency. *Advanced Energy Materials*, 12: 2270092.

[51] Choi, Y., Koo, D., Jeong, M., Jeong, G., Lee, J., Lee, B., Choi, K. J., Yang, C., Park, H. (2021). Toward all-vacuum-processable perovskite solar cells with high efficiency, stability, and scalability enabled by fluorinated spiro-OMeTAD through thermal evaporation. *Solar RRL*, 5: 2100415.

[52] Ji, R., Zhang, Z. B., Cho, C., An, Q. Z., Paulus, F., Kroll, M., Löffler, M., Nehm, F., Rellinghaus, B., Leo, K., et al. (2020). Thermally evaporated methylammonium-free perovskite solar cells. *Journal of Materials Chemistry C*, 8: 7725–7733.

[53] Tavakoli, M. M., Tavakoli, R. (2021). All-vacuum-processing for fabrication of efficient, large-scale, and flexible inverted perovskite solar cells. *Physica Status Solidi (RRL) – Rapid Research Letters*, 15: 2000449.

[54] Wang, Q. R., Lin, Z. H., Su, J., Hu, Z. S., Chang, J. J., Hao, Y. (2021). Recent progress of inorganic hole transport materials for efficient and stable perovskite solar cells. *Nano Select*, 2: 1055–1080.

[55] Ke, W. J., Zhao, D. W., Grice, C. R., Cimaroli, A. J., Fang, G. J., Yan, Y. F. (2015). Efficient fully-vacuum-processed perovskite solar cells using copper phthalocyanine as hole selective layers. *Journal of Materials Chemistry A*, 3: 23888–23894.

[56] Guo, Y. X., Lei, H. W., Xiong, L. B., Li, B. R., Fang, G. J. (2018). An integrated organic-inorganic hole transport layer for efficient and stable perovskite solar cells. *Journal of Materials Chemistry A*, 6: 2157–2165.

[57] Momblona, C., Gil-Escrig, L., Bandiello, E., Hutter, E. M., Sessolo, M., Lederer, K., Blochwitz-Nimoth, J., Bolink, H. J. (2016). Efficient vacuum deposited p-i-n and n-i-p perovskite solar cells employing doped charge transport layers. *Energy & Environmental Science*, 9: 3456–3463.

[58] Pérez-Del-Rey, D., Boix, P. P., Sessolo, M., Hadipour, A., Bolink, H. J. (2018). Interfacial modification for high-efficiency vapor-phase-deposited perovskite solar cells based on a metal oxide buffer layer. *The Journal of Physical Chemistry Letters*, 9: 1041–1046.

[59] Leyden, M. R., Ono, L. K., Raga, S. R., Kato, Y., Wang, S. H., Qi, Y. B. (2014). High performance perovskite solar cells by hybrid chemical vapor deposition. *Journal of Materials Chemistry A*, 2: 18742–18745.

[60] Qiu, L. B., He, S. S., Jiang, Y., Son, D. Y., Ono, L. K., Liu, Z. H., Kim, T., Bouloumis, T., Kazaoui, S., Qi, Y. B. (2019). Hybrid chemical vapor deposition enables scalable and stable Cs-FA mixed cation perovskite solar modules with a designated area of 91.8 cm² approaching 10% efficiency. *Journal of Materials Chemistry A*, 7: 6920–6929.

[61] Liu, J. J., Shi, B., Xu, Q. J., Li, Y. C., Chen, B. B., Wang, Q., Wang, P. Y., Zhao, Y., Zhang, X. D. (2021). Crystalline quality control in sequential vapor deposited perovskite film toward high efficiency and large scale solar cells. *Solar Energy Materials and Solar Cells*, 233: 111382.

[62] Jiang, Y., Remeika, M., Hu, Z. H., Juarez-Perez, E. J., Qiu, L. B., Liu, Z. H., Kim, T., Ono, L. K., Son, D. Y., Hawash, Z., et al. (2019). Negligible-Pb-waste and upscalable perovskite deposition technology for high-operational-stability perovskite solar modules. *Advanced Energy Materials*, 9: 1803047.

[63] Qiu, L. B., He, S. S., Liu, Z. H., Ono, L. K., Son, D. Y., Liu, Y. Q., Tong, G. Q., Qi, Y. B. (2020). Rapid hybrid chemical vapor deposition for efficient and hysteresis-free perovskite solar modules with an operation lifetime exceeding 800 hours. *Journal of Materials Chemistry A*, 8: 23404–23412.

[64] Smirnov, Y., Schmengler, L., Kuik, R., Repecaud, P. A., Najafi, M., Zhang, D., Theelen, M., Aydin, E., Veenstra, S., De Wolf, S., et al. (2021). Scalable pulsed laser deposition of transparent rear electrode for perovskite solar cells. *Advanced Materials Technologies*, 6: 2000856.

[65] Raiford, J. A., Oyakhire, S. T., Bent, S. F. (2020). Applications of atomic layer deposition and chemical vapor deposition for perovskite solar cells. *Energy & Environmental Science*, 13: 1997–2023.

[66] Zhou, J., Tian, X. Y., Wang, B. K., Zhang, S. S., Liu, Z. H., Chen, W. (2022). Application of low temperature atomic layer deposition packaging technology in OLED and its implications for organic and perovskite solar cell packaging. *Acta Chimica Sinica*, 80: 395.

[67] Lv, Y. F., Xu, P. H., Ren, G. Q., Chen, F., Nan, H. R., Liu, R. Q., Wang, D., Tan, X., Liu, X. Y., Zhang, H., et al. (2018). Low-temperature atomic layer deposition of metal oxide layers for perovskite solar cells with high efficiency and stability under harsh environmental conditions. *ACS Applied Materials & Interfaces*, 10: 23928–23937.

[68] Altinkaya, C., Aydin, E., Ugur, E., Isikgor, F. H., Subbiah, A. S., De Bastiani, M., Liu, J., Babayigit, A., Allen, T. G., Laquai, F., et al. (2021). Tin oxide electron-selective layers for efficient, stable, and scalable perovskite solar cells. *Advanced Materials*, 33: 2005504.

[69] Qiu, L. B., Ono, L. K., Jiang, Y., Leyden, M. R., Raga, S. R., Wang, S. H., Qi, Y. B. (2018). Engineering interface structure to improve efficiency and stability of organometal halide perovskite solar cells. *The Journal of Physical Chemistry B*, 122: 511–520.

[70] Lee, Y. H., Lee, S., Seo, G., Paek, S., Cho, K. T., Huckaba, A. J., Calizzi, M., Choi, D. W., Park, J. S., Lee, D., et al. (2018). Efficient planar perovskite solar cells using passivated tin oxide as an electron transport layer. *Advanced Science*, 5: 1800130.

[71] Correa Baena, J. P., Steier, L., Tress, W., Saliba, M., Neutzner, S., Matsui, T., Giordano, F., Jacobsson, T. J., Srimath Kandada, A. R., Zakeeruddin, S. M., et al. (2015). Highly efficient planar perovskite solar cells through band alignment engineering. *Energy & Environmental Science*, 8: 2928–2934.

[72] Correa-Baena, J. P., Tress, W., Domanski, K., Anaraki, E. H., Turren-Cruz, S. H., Roose, B., Boix, P. P., Grätzel, M., Saliba, M., Abate, A., et al. (2017). Identifying and suppressing interfacial recombination to achieve high open-circuit voltage in perovskite solar cells. *Energy & Environmental Science*, 10: 1207–1212.

[73] Wang, C. L., Zhao, D. W., Grice, C. R., Liao, W. Q., Yu, Y., Cimaroli, A., Shrestha, N., Roland, P. J., Chen, J., Yu, Z. H., et al. (2016). Low-temperature plasma-enhanced atomic layer deposition of tin oxide electron selective layers for highly efficient planar per-

ovskite solar cells. *Journal of Materials Chemistry A*, 4: 12080–12087.

[74] Seo, S., Park, I. J., Kim, M., Lee, S., Bae, C., Jung, H. S., Park, N. G., Kim, J. Y., Shin, H. (2016). An ultra-thin, un-doped NiO hole transporting layer of highly efficient (16.4%) organic-inorganic hybrid perovskite solar cells. *Nanoscale*, 8: 11403–11412.

[75] Xiao, K., Lin, R. X., Han, Q. L., Hou, Y., Qin, Z. Y., Nguyen, H. T., Wen, J., Wei, M. Y., Yeddu, V., Saidaminov, M. I., et al. (2020). All-perovskite tandem solar cells with 24.2% certified efficiency and area over 1 cm2 using surface-anchoring zwitterionic antioxidant. *Nature Energy*, 5: 870–880.

[76] Zhu, S. J., Yao, X., Ren, Q. S., Zheng, C. C., Li, S. Z., Tong, Y. P., Shi, B., Guo, S., Fan, L., Ren, H. Z., et al. (2018). Transparent electrode for monolithic perovskite/silicon-heterojunction two-terminal tandem solar cells. *Nano Energy*, 45: 280–286.

[77] Palmstrom, A. F., Eperon, G. E., Leijtens, T., Prasanna, R., Habisreutinger, S. N., Nemeth, W., Gaulding, E. A., Dunfield, S. P., Reese, M., Nanayakkara, S., et al. (2019). Enabling flexible all-perovskite tandem solar cells. *Joule*, 3: 2193–2204.

[78] Lu, Q., Yang, Z. C., Meng, X., Yue, Y. F., Ahmad, M. A., Zhang, W. J., Zhang, S. S., Zhang, Y. Q., Liu, Z. H., Chen, W. (2021). A review on encapsulation technology from organic light emitting diodes to organic and perovskite solar cells. *Advanced Functional Materials*, 31: 2100151.

[79] Choi, E. Y., Kim, J., Lim, S., Han, E., Ho-Baillie, A. W. Y., Park, N. (2018). Enhancing stability for organic-inorganic perovskite solar cells by atomic layer deposited Al$_2$O$_3$ encapsulation. *Solar Energy Materials and Solar Cells*, 188: 37–45.

[80] Ramos, F. J., Maindron, T., Béchu, S., Rebai, A., Frégnaux, M., Bouttemy, M., Rousset, J., Schulz, P., Schneider, N. (2018). Versatile perovskite solar cell encapsulation by low-temperature ALD-Al$_2$O$_3$ with long-term stability improvement. *Sustainable Energy & Fuels*, 2: 2468–2479.

[81] Lee, Y. I., Jeon, N. J., Kim, B. J., Shim, H., Yang, T. Y., Seok, S. I., Seo, J., Im, S. G. (2018). A low-temperature thin-film encapsulation for enhanced stability of a highly efficient perovskite solar cell. *Advanced Energy Materials*, 8: 1701928.

[82] Yin, X. T., Guo, Y. X., Xie, H. X., Que, W. X., Kong, L. B. (2019). Nickel oxide as efficient hole transport materials for perovskite solar cells. *Solar RRL*, 3: 1900001.

[83] Li, G. J., Jiang, Y. B., Deng, S. B., Tam, A., Xu, P., Wong, M., Kwok, H. S. (2017). Overcoming the limitations of sputtered nickel oxide for high-efficiency and large-area perovskite solar cells. *Advanced Science*, 4: 1700463.

[84] Bai, G. F., Wu, Z. L., Li, J., Bu, T. L., Li, W. N., Li, W., Huang, F. Z., Zhang, Q., Cheng, Y. B., Zhong, J. (2019). High performance perovskite sub-module with sputtered SnO$_2$ electron transport layer. *Solar Energy*, 183: 306–314.

[85] Qiu, L. B., Liu, Z. H., Ono, L. K., Jiang, Y., Son, D. Y., Hawash, Z., He, S. S., Qi, Y. B. (2019). Scalable fabrication of stable high efficiency perovskite solar cells and modules utilizing room temperature sputtered SnO$_2$ electron transport layer. *Advanced Functional Materials*, 29: 1806779.

[86] Aydin, E., Altinkaya, C., Smirnov, Y., Yaqin, M. A., Zanoni, K. P. S., Paliwal, A., Firdaus, Y., Allen, T. G., Anthopoulos, T. D., Bolink, H. J., et al. (2021). Sputtered transparent electrodes for optoelectronic devices: Induced damage and mitigation strategies. *Matter*, 4: 3549–3584.

[87] Lim, S. H., Seok, H. J., Kwak, M. J., Choi, D. H., Kim, S. K., Kim, D. H., Kim, H. K. (2021). Semi-transparent perovskite solar cells with bidirectional transparent electrodes. *Nano Energy*, 82: 105703.

[88] Wei, Z. F., Smith, B., De Rossi, F., Searle, J. R., Worsley, D. A., Watson, T. M. (2019). Efficient and semi-transparent perovskite solar cells using a room-temperature processed MoO$_x$/ITO/Ag/ITO electrode. *Journal of Materials Chemistry C*, 7: 10981–10987.

[89] Gao, B., Hu, J., Tang, S., Xiao, X. Y., Chen, H., Zuo, Z., Qi, Q., Peng, Z. Y., Wen, J. C., Zou, D. C. (2021). Organic-inorganic perovskite films and efficient planar heterojunction solar cells by mag-

netron sputtering. *Advanced Science*, 8: e2102081.

[90] Gao, B., Hu, J., Zuo, Z., Qi, Q., Peng, Z. Y., Chen, H., Yan, K., Hou, S. C., Zou, D. C. (2022). Doping mechanism of perovskite films with PbCl$_2$ prepared by magnetron sputtering for enhanced efficiency of solar cells. *ACS Applied Materials & Interfaces*, 14: 40062–40071.

[91] Xu, F., Li, Y. J., Yuan, B. L., Zhang, Y. Z., Wei, H. M., Wu, Y. Q., Cao, B. Q. (2021). Large-area CsPbBr$_3$ perovskite films grown with effective one-step RF-magnetron sputtering. *Journal of Applied Physics*, 129: 245303.

[92] VacCoat (2022). What is pulsed laser deposition (PLD)? Available at https://vaccoat.com/blog/what-is-pulsed-laser-deposition-pld/.

[93] European Synchrotron Radiation Facility. Pulsed laser deposition. Available at: https://www.esrf.fr/UsersAndScience/Experiments/CRG/BM25/inhouseresearch/supportlaboratory/PLD.

[94] Smirnov, Y., Repecaud, P. A., Tutsch, L., Florea, I., Zanoni, K. P. S., Paliwal, A., Bolink, H. J., i Cabarrocas, P. R., Bivour, M., Morales-Masis, M. (2022). Wafer-scale pulsed laser deposition of ITO for solar cells: Reduced damage *vs*. interfacial resistance. *Materials Advances*, 3: 3469–3478.

[95] Zanoni, K. P. S., Paliwal, A., Hernández-Fenollosa, M. A., Repecaud, P. A., Morales-Masis, M., Bolink, H. J. (2022). ITO top-electrodes via industrial-scale PLD for efficient buffer-layer-free semitransparent perovskite solar cells. *Advanced Materials Technologies*, 7: 2101747.

[96] Park, J. H., Seo, J., Park, S., Shin, S. S., Kim, Y. C., Jeon, N. J., Shin, H. W., Ahn, T. K., Noh, J. H., Yoon, S. C., et al. (2015). Efficient CH$_3$NH$_3$PbI$_3$ perovskite solar cells employing nanostructured p-type NiO electrode formed by a pulsed laser deposition. *Advanced Materials*, 27: 4013–4019.

[97] Qiu, Z. W., Gong, H. B., Zheng, G., Yuan, S., Zhang, H. L., Zhu, X. M., Zhou, H. P., Cao, B. Q. (2017). Enhanced physical properties of pulsed laser deposited NiO films *via* annealing and lithium doping for improving perovskite solar cell efficiency. *Journal of Materials Chemistry C*, 5: 7084–7094.

[98] Feng, M. L., Wang, M., Zhou, H. P., Li, W., Wang, S. P., Zang, Z. G., Chen, S. J. (2020). High-efficiency and stable inverted planar perovskite solar cells with pulsed laser deposited Cu-doped NiO$_x$ hole-transport layers. *ACS Applied Materials & Interfaces*, 12: 50684–50691.

[99] Ke, S. M., Du, B. K., Rao, Z. G., Huang, C., Lin, P., Hu, Y. M., Shu, L. L. (2019). Pulsed laser deposition of amorphous InGaZnO$_4$ as an electron transport layer for perovskite solar cells. *Journal of Advanced Dielectrics*, 9: 1950042.

[100] Gao, Y. B., Wu, Y. J., Liu, Y., Chen, C., Shen, X. Y., Bai, X., Shi, Z. F., Yu, W. W., Dai, Q. L., Zhang, Y. (2019). Improved interface charge extraction by double electron transport layers for high-efficient planar perovskite solar cells. *Solar RRL*, 3: 1900314.

[101] Zhang, H., Wang, H., Ma, M. Y., Wu, Y., Dong, S., Xu, Q. Y. (2018). Application of compact TiO$_2$ layer fabricated by pulsed laser deposition in organometal trihalide perovskite solar cells. *Solar RRL*, 2: 1800097.

[102] Dunlap-Shohl, W. A., Barraza, E. T., Barrette, A., Gundogdu, K., Stiff-Roberts, A. D., Mitzi, D. B. (2018). MAPbI$_3$ solar cells with absorber deposited by resonant infrared matrix-assisted pulsed laser evaporation. *ACS Energy Letters*, 3: 270–275.

[103] Bansode, U., Naphade, R., Game, O., Agarkar, S., Ogale, S. (2015). Hybrid perovskite films by a new variant of pulsed excimer laser deposition: A room-temperature dry process. *The Journal of Physical Chemistry C*, 119: 9177–9185.

[104] Bansode, U., Ogale, S. (2017). On-axis pulsed laser deposition of hybrid perovskite films for solar cell and broadband photo-sensor applications. *Journal of Applied Physics*, 121: 133107.

[105] Soto-Montero, T., Soltanpoor, W., Kralj, S., Birkhölzer, Y. A., Remes, Z., Ledinsky, M., Rijnders, G., Morales-Masis, M. (2021). Single-source pulsed laser deposition of MAPbI$_3$. In: Proceedings of the 2021 IEEE 48th Photovoltaic Specialists Conference (PVSC), Fort Lauderdale, FL, USA.

[106] Wang, H., Wu, Y., Ma, M. Y., Dong, S., Li, Q., Du, J., Zhang, H., Xu, Q. Y. (2019). Pulsed laser deposition of CsPbBr₃ films for application in perovskite solar cells. *ACS Applied Energy Materials*, 2: 2305–2312.

[107] Jin, X., Song, S. X., Liu, Z., Wang, H., Wang, B., Guan, J., Zhang, H., Xu, Q. Y. (2021). High-stability patterned CsPbIxBr₃₋ₓ thin films with tunable crystal size prepared by solid-phase reaction. *Advanced Optical Materials*, 9: 2101175.

[108] Hoffmann-Urlaub, S., Zhang, Y. D., Wang, Z. D., Kressdorf, B., Meyer, T. (2020). Fabrication of tin-based halide perovskites by pulsed laser deposition. *Applied Physics A*, 126: 335.

[109] Kiyek, V. M., Birkhölzer, Y. A., Smirnov, Y., Ledinsky, M., Remes, Z., Momand, J., Kooi, B. J., Koster, G., Rijnders, G., Morales-Masis, M. (2020). Single-source, solvent-free, room temperature deposition of black γ-CsSnI₃ films. *Advanced Materials Interfaces*, 7: 2000162.

[110] Rodkey, N., Kaal, S., Sebastia-Luna, P., Birkhölzer, Y. A., Ledinsky, M., Palazon, F., Bolink, H. J., Morales-Masis, M. (2021). Pulsed laser deposition of Cs₂AgBiBr₆: From mechanochemically synthesized powders to dry, single-step deposition. *Chemistry of Materials*, 33: 7417–7422.

[111] Schulze, P. S. C., Bett, A. J., Winkler, K., Hinsch, A., Lee, S., Mastroianni, S., Mundt, L. E., Mundus, M., Würfel, U., Glunz, S. W., et al. (2017). Novel low-temperature process for perovskite solar cells with a mesoporous TiO₂ scaffold. *ACS Applied Materials & Interfaces*, 9: 30567–30574.

[112] Liu, L. L., Yang, S. E., Liu, P., Chen, Y. S. (2022). High-quality and full-coverage CsPbBr₃ thin films via electron beam evaporation with post-annealing treatment for all-inorganic perovskite solar cells. *Solar Energy*, 232: 320–327.

[113] Qiu, W. M., Paetzold, U. W., Gehlhaar, R., Smirnov, V., Boyen, H. G., Tait, J. G., Conings, B., Zhang, W. M., Nielsen, C. B., McCulloch, I., et al. (2015). An electron beam evaporated TiO₂ layer for high efficiency planar perovskite solar cells on flexible polyethylene terephthalate substrates. *Journal of Materials Chemistry A*, 3: 22824–22829.

[114] Li, Y. B., Cooper, J. K., Liu, W. J., Sutter-Fella, C. M., Amani, M., Beeman, J. W., Javey, A., Ager, J. W., Liu, Y., Toma, F. M., et al.

[115] Ma, J. J., Zheng, X. L., Lei, H. W., Ke, W. J., Chen, C., Chen, Z. L., Yang, G., Fang, G. J. (2017). Highly efficient and stable planar perovskite solar cells with large-scale manufacture of E-beam evaporated SnO₂ toward commercialization. *Solar RRL*, 1: 1700118.

[116] Blackburn, D., Routledge, T. J., O'Kane, M., Cassella, E. J., Game, O. S., Catley, T. E., Wood, C. J., McArdle, T., Lidzey, D. G. (2022). Low-temperature, scalable, reactive deposition of tin oxide for perovskite solar cells. *Solar RRL*, 6: 2270081.

[117] Feng, J. S., Yang, Z., Yang, D., Ren, X. D., Zhu, X. J., Jin, Z. W., Zi, W., Wei, Q. B., Liu, S. Z. (2017). E-beam evaporated Nb₂O₅ as an effective electron transport layer for large flexible perovskite solar cells. *Nano Energy*, 36: 1–8.

[118] Abzieher, T., Schwenzer, J. A., Moghadamzadeh, S., Sutterluti, F., Hossain, I. M., Pfau, M., Lotter, E., Hetterich, M., Richards, B. S., Lemmer, U., et al. (2019). Efficient all-evaporated *pin*-perovskite solar cells: A promising approach toward industrial large-scale fabrication. *IEEE Journal of Photovoltaics*, 9: 1249–1257.

[119] Abzieher, T., Moghadamzadeh, S., Schackmar, F., Eggers, H., Sutterlüti, F., Farooq, A., Kojda, D., Habicht, K., Schmager, R., Mertens, A., et al. (2019). Photovoltaic devices: Electron-beam-evaporated nickel oxide hole transport layers for perovskite-based photovoltaics. *Advanced Energy Materials*, 9: 1970035.

[120] Liu, X., Jiang, J., Wang, F., Xiao, Y., Sharp, I. D., Li, Y. (2019). High photovoltage inverted planar heterojunction perovskite solar cells with all-inorganic selective contact layers. *ACS Applied Materials & Interfaces*, 11: 46894–46901.

[121] Jiang, J. X., Mavrič, A., Pastukhova, N., Valant, M., Zeng, Q. G., Fan, Z. Y., Zhang, B. B., Li, Y. B. (2022). Coevaporation of doped inorganic carrier-selective layers for high-performance inverted planar perovskite solar cells. *Solar RRL*, 6: 2200091.

[122] Du, M. Y., Zhao, S., Duan, L. J., Cao, Y. X., Wang, H., Sun, Y. M., Wang, L. K., Zhu, X. J., Feng, J. S., Liu, L., et al. (2022). Surface redox engineering of vacuum-deposited NiOₓ for top-performance perovskite solar cells and modules. *Joule*, 6: 1931–1943.

(2016). Defective TiO₂ with high photoconductive gain for efficient and stable planar heterojunction perovskite solar cells. *Nature Communications*, 7: 12446.